CrossMark

LOW-FREQUENCY OBSERVATIONS OF LINEARLY POLARIZED STRUCTURES IN THE INTERSTELLAR MEDIUM NEAR THE SOUTH GALACTIC POLE

E. Lenc[1,2], B. M. Gaensler[1,2,3], X. H. Sun[1], E. M. Sadler[1,2], A. G. Willis[4], N. Barry[5], A. P. Beardsley[5,6], M. E. Bell[2,7], G. Bernardi[8], J. D. Bowman[6], F. Briggs[2,9], J. R. Callingham[1,2,7], R. J. Cappallo[10], P. Carroll[5], B. E. Corey[10], A. de Oliveira-Costa[11], A. A. Deshpande[12], J. S. Dillon[11,13], K. S. Dwarkanath[12], D. Emrich[14], A. Ewall-Wice[11], L. Feng[11], B.-Q. For[15], R. Goeke[11], L. J. Greenhill[16], P. Hancock[2,14], B. J. Hazelton[5,17], J. N. Hewitt[11], L. Hindson[18], N. Hurley-Walker[14], M. Johnston-Hollitt[18], D. C. Jacobs[6], A. D. Kapińska[2,15], D. L. Kaplan[19], J. C. Kasper[16,20], H.-S. Kim[2,21], E. Kratzenberg[10], J. Line[2,21], A. Loeb[16], C. J. Lonsdale[10], M. J. Lynch[14], B. McKinley[21], S. R. McWhirter[10], D. A. Mitchell[2,7], M. F. Morales[5], E. Morgan[11], J. Morgan[2,14], T. Murphy[1,2], A. R. Neben[11], D. Oberoi[22], A. R. Offringa[23], S. M. Ord[2,7], S. Paul[12], B. Pindor[2,21], J. C. Pober[24], T. Prabu[12], J. Riding[2,21], A. E. E. Rogers[10], A. Roshi[25], N. Udaya Shankar[12], S. K. Sethi[12], K. S. Srivani[12], L. Staveley-Smith[2,15], R. Subrahmanyan[2,12], I. S. Sullivan[5], M. Tegmark[11], Nithyanandan Thyagarajan[6], S. J. Tingay[2,14,26], C. Trott[2,14], M. Waterson[9,14], R. B. Wayth[2,14], R. L. Webster[2,21], A. R. Whitney[10], A. Williams[14], C. L. Williams[11], C. Wu[15], J. S. B. Wyithe[2,21], and Q. Zheng[18]

[1] Sydney Institute for Astronomy, School of Physics, The University of Sydney, NSW 2006, Australia
[2] ARC Centre of Excellence for All-sky Astrophysics (CAASTRO), Australia
[3] Dunlap Institute for Astronomy and Astrophysics, University of Toronto, 50 St. George Street, Toronto, ON M5S 3H4, Canada
[4] National Research Council of Canada, Herzberg Astronomy and Astrophysics, P.O. Box 248, Penticton, BC, Canada
[5] Department of Physics, University of Washington, Seattle, WA 98195, USA
[6] School of Earth and Space Exploration, Arizona State University, Tempe, AZ 85287, USA
[7] CSIRO Astronomy and Space Science (CASS), P.O. Box 76, Epping, NSW 1710, Australia
[8] Department of Physics and Electronics, Rhodes University, P.O. Box 94, Grahamstown 6140, South Africa
[9] Research School of Astronomy and Astrophysics, Australian National University, Canberra, ACT 2611, Australia
[10] MIT Haystack Observatory, Westford, MA 01886, USA
[11] MIT Kavli Institute for Astrophysics and Space Research, Massachusetts Institute of Technology, Cambridge, MA 02139, USA
[12] Raman Research Institute, Bangalore 560080, India
[13] Department of Astronomy, University of California, Berkeley, CA 94720, USA
[14] International Centre for Radio Astronomy Research, Curtin University, Bentley, WA 6102, Australia
[15] ICRAR University of Western Australia, Crawley, WA 6009, Australia
[16] Harvard-Smithsonian Center for Astrophysics, Cambridge, MA 02138, USA
[17] University of Washington, eScience Institute, Seattle, WA 98195, USA
[18] School of Chemical & Physical Sciences, Victoria University of Wellington, Wellington 6140, New Zealand
[19] Department of Physics, University of Wisconsin–Milwaukee, Milwaukee, WI 53201, USA
[20] University of Michigan, Department of Atmospheric, Oceanic and Space Sciences, Ann Arbor, MI 48109, USA
[21] School of Physics, The University of Melbourne, Parkville, VIC 3010, Australia
[22] National Centre for Radio Astrophysics, Tata Institute for Fundamental Research, Pune 411007, India
[23] ASTRON, The Netherlands Institute for Radio Astronomy, Postbus 2, 7990 AA, Dwingeloo, The Netherlands
[24] Brown University, Department of Physics, Providence, RI 02912, USA
[25] National Radio Astronomy Observatory, Charlottesville and Greenbank, USA
[26] Osservatorio di Radio Astronomia, Istituto Nazionale di Astrofisica, Bologna, I-40123, Italy

ABSTRACT

We present deep polarimetric observations at 154 MHz with the Murchison Widefield Array (MWA), covering 625 $\deg^2$ centered on $\alpha = 0^h$ and $\delta = -27°$. The sensitivity available in our deep observations allows an in-band, frequency-dependent analysis of polarized structure for the first time at long wavelengths. Our analysis suggests that the polarized structures are dominated by intrinsic emission but may also have a foreground Faraday screen component. At these wavelengths, the compactness of the MWA baseline distribution provides excellent snapshot sensitivity to large-scale structure. The observations are sensitive to diffuse polarized emission at $\sim54'$ resolution with a sensitivity of 5.9 mJy beam^{-1} and compact polarized sources at $\sim2.'4$ resolution with a sensitivity of 2.3 mJy beam^{-1} for a subset (400 $\deg^2$) of this field. The sensitivity allows the effect of ionospheric Faraday rotation to be spatially and temporally measured directly from the diffuse polarized background. Our observations reveal large-scale structures ($\sim1°-8°$ in extent) in linear polarization clearly detectable in ~2 minute snapshots, which would remain undetectable by interferometers with minimum baseline lengths of >110 m at 154 MHz. The brightness temperature of these structures is on average 4 K in polarized intensity, peaking at 11 K. Rotation measure synthesis reveals that the structures have Faraday depths ranging from -2 to 10 rad m^{-2} with a large fraction peaking at approximately $+1$ rad m^{-2}. We estimate a distance of 51 ± 20 pc to the polarized emission based on measurements of the in-field pulsar J2330–2005. We detect four extragalactic linearly polarized point sources within the field in our compact source survey. Based on the known polarized source population at 1.4 GHz and non-detections at 154 MHz, we estimate an upper limit on the depolarization ratio of 0.08 from 1.4 GHz to 154 MHz.

1. INTRODUCTION

The interstellar medium (ISM) of the Milky Way hosts a variety of physical mechanisms that define the structure and evolution of the Galaxy. It is a multi-phase medium composed of a tenuous plasma that is permeated by a large-scale magnetic field and is highly turbulent (McKee & Ostriker 2007; Haverkorn et al. 2015). Despite advances in theory and simulation (Burkhart et al. 2012), our understanding of the properties of the ISM has been limited by the dearth of observational data against which to test.

The local ISM, particularly within the local bubble (Lallement et al. 2003), has been very poorly studied. Studies using multi-wavelength observations of diffuse emission (Puspitarini et al. 2014) show that the local bubble appears to be open-ended toward the south galactic pole (SGP). Polarimetry from stars can be a useful probe (Berdyugin & Teerikorpi 2001; Berdyugin et al. 2004, 2014); however, these are sparsely sampled for stars within the local bubble region (a few tens of parsecs to ~100 pc). Observations of pulsars can also be used to probe conditions in the line of sight to the source (Mao et al. 2010); however, the density of such sources is low, even more so if only nearby sources are considered and for directions at mid or high Galactic latitudes.

Radio observations of diffuse polarized emission have become a valuable tool for understanding the structure and properties of the ISM. At 350 MHz, it has been demonstrated that diffuse polarization could result from gradients in the rotation measure (RM) and that they could be used to study the structure of the diffuse ionized gas (Wieringa et al. 1993; Haverkorn et al. 2000; Haverkorn & Heitsch 2004). Gaensler et al. (2011) observed features at 1.4 GHz associated with the turbulent ISM using polarization gradient maps. Such features have also been observed as part of the Canadian Galactic Place Survey at 1.4 GHz (Taylor et al. 2003) carried out at the Dominion Radio Astrophysical Observatory, the S-band Polarization All Sky Survey (S-PASS) at 2.3 GHz with the Parkes radio telescope (Carretti 2010; Iacobelli et al. 2014) and at 4.8 GHz at Urumqi as part of the Sino-German λ6 cm Polarization Survey of the Galactic Plane (Sun et al. 2011, 2014; Han et al. 2013). These centimeter-wavelength observations are significantly less affected by depth depolarization than longer wavelength ones and can probe the ISM out to kiloparsec distances. However, because they are also sensitive to the local ISM, they cannot distinguish between nearby structures and more distant ones. Longer wavelength observations provide a means to do so; depth depolarization is so significant at these wavelengths that only local regions of the ISM can be seen. As such, they provide a valuable tool for probing the local ISM.

Long wavelength polarimetric observations are particularly sensitive to small changes in Faraday rotation, as a result of fluctuations in the magnetized plasma, which are difficult to detect at shorter wavelengths. Several such studies have been performed with synthesis telescopes at long wavelengths, e.g., the Westerbork Synthesis Radio Telescope (WSRT) between 325 and 375 MHz (Wieringa et al. 1993; Haverkorn et al. 2000, 2003a, 2003b, 2003c), WSRT at 150 MHz (Bernardi

et al. 2009, 2010; Iacobelli et al. 2013), LOFAR at 150 MHz (Jelić et al. 2014) and at 189 MHz with a Murchison Widefield Array (MWA) prototype (Bernardi et al. 2013), but none of these were sensitive to structures larger than ~1°. LOFAR observations of the 3C196 field at 150 MHz (Jelić et al. 2015) achieved sensitivity to spatial scales up to ~5° by utilizing a dual-inner-HBA mode (van Haarlem et al. 2013). However, only a limited number of short-baselines are available in this mode and sensitivity is compromised to provide them. Single dish polarimetric observations at long wavelengths provide access to large-scale structure but so far there has only been one such observation (Mathewson & Milne 1965) and it suffered from poor sensitivity and spatial sampling. Furthermore, single dish observations below 300 MHz also lack resolution.

The MWA can help to bridge the gap that exists between existing single-dish and interferometric observations at long wavelengths. The MWA is a low-frequency (72–300 MHz) interferometer located in Western Australia (Tingay et al. 2013), with four key science themes: (1) searching for emission from the epoch of reionization (EoR); (2) Galactic and extragalactic surveys; (3) transient science; and (4) solar, heliospheric, and ionospheric science and space weather (Bowman et al. 2013). The array has a very wide field of view (over 600 deg² at 154 MHz) and the dense compact distribution of baselines provides excellent sensitivity to structure on scales up to 14° in extent at 154 MHz. Most importantly for this project, the high sensitivity observations can, for the first time, enable a frequency-dependent analysis of large-scale polarized structure. The large number of baselines provide high sensitivity (~100 mJy rms for a 1 s integration) and dense (u, v)-coverage for snapshot imaging. Visibilities can be generated with a spectral resolution of 10 kHz and with cadences as low as 0.5 s with the current MWA correlator (Ord et al. 2015); however, typical imaging is performed on >112 s timescales.

In this paper, we present results from the first deep MWA survey of diffuse polarization and polarized point sources, for an EoR field situated just west of the SGP. The primary aims of the survey are to study polarized structures in the local ISM, localize them, and gain insights into the processes that generate them. Secondary aims include a study of the polarized point-source population at long wavelengths and also an overall evaluation of the polarimetric capabilities of the MWA.

In Section 2, we describe the MWA observations and data reduction. In Section 3, we present our diffuse total intensity and polarization maps, apply RM synthesis, analyze the effects of the ionosphere on the observed Faraday rotation, create both continuum and frequency-dependent polarization gradient maps, and search for polarized point sources. In Section 4, we explore the nature of the diffuse polarization, estimate the distance to the observed polarized features, study the linearly polarized point-source population, discuss possible causes for the polarized structures based on frequency-dependent observations, perform a structure function analysis, and study the observed Faraday depth spectra. A summary and conclusion are provided in Section 5.

Table 1
Details of MWA Polarization Observations in the EoR-0 Field

Epoch	Project	R.A.	decl.	Obs. Date	Start Time (UTC)	End Time (UTC)	N_{obs}[a]	Band (MHz)	t_{int}[b] (s)
1	EoR	$0^h00^m00^s.00$	$-27°00'00''.0$	2013 Aug 26	15:04:08	18:27:28	44	138.88–169.60	0.5
2(a)	GLEAM	$0^h03^m16^s.01$	$-26°46'49''.1$	2013 Nov 25	11:58:56	12:00:48	1	138.88–169.60	0.5
2(b)	GLEAM	$0^h05^m16^s.41$	$-26°46'48''.7$	2013 Nov 25	12:00:56	12:02:48	1	169.60–200.32	0.5
2(c)	GLEAM	$0^h07^m16^s.81$	$-26°46'48''.7$	2013 Nov 25	12:02:56	12:04:48	1	200.32–231.04	0.5
3	EoR	$0^h00^m00^s.00$	$-27°00'00''.0$	2014 Nov 06	12:56:32	14:09:44	36	138.88–169.60	2.0

Notes.
[a] Total number of 112 s snapshots used from observation.
[b] Visibility integration time.

2. OBSERVATIONS AND DATA REDUCTION

All observations were carried out with the 128 tile MWA, located at the Murchison Radio Observatory in Western Australia. Each tile consists of a regular 4×4 grid of dual-polarization dipoles. The dipole signals are combined in an analog beamformer, using a set of switchable delay lines, to form a tile beam.

More specifically, data for this investigation were obtained from observations associated with MWA proposals G0008 GLEAM (A Galactic and Extragalactic All-Sky MWA Survey) and G0009 EoR (Epoch of Reionization).[27] The two projects utilize two different observing strategies; GLEAM (Wayth et al. 2015, and Hurley-Walker et al. 2016) uses a drift-scan observing mode, i.e., the tiles always point to the meridian, whereas the EoR observations track the field over ∼4 hr with quantized beamformer settings that are separated by about 7° (Paul et al. 2014; Trott 2014; Jacobs et al. 2016). The EoR observations enable deep scans of individual fields, whereas the GLEAM observations minimize instrumental systematics by maintaining a consistent observing set up. While the GLEAM observations are not as deep as the EoR observations, they are observed in multiple 30.72 MHz frequency bands and thus enable frequency-dependent polarization characteristics to be explored over a wider range of wavelengths.

While a vast quantity of EoR and GLEAM data has already been collected, our investigation here primarily focuses on the MWA EoR-0 field, which is centered on $\alpha = 0^h$, $\delta = -27°$, approximately 10° west of the SGP ($b = -90°$). Only a small subset of the available data has been used in this initial study of the characteristics of linearly polarized diffuse emission in this region. Specifically, two epochs of 154 MHz EoR data (so-called "low-band" by the MWA EoR community) and one epoch of multi-band GLEAM data (centered on 154, 185, and 216 MHz), which contains the EoR-0 region, have been selected. A summary of parameters associated with the three epochs of observations used in this investigation can be found in Table 1. The epoch 1 EoR data corresponds to a quiet period in the ionosphere whereas epoch 3 coincides with the arrival of a coronal mass ejection that propagated from the Sun (Kaplan et al. 2015) and interacted with the ionosphere. For polarimetric studies, our interest is primarily in the 154 MHz data (low-band EoR data) because this band is less prone to polarization leakage than at higher frequencies, where inaccuracies in the MWA beam model become significant (Sutinjo et al. 2015).

For the EoR and GLEAM observations, the MWA correlator was configured to generate visibilities in 24 coarse channels, each with 32×40 kHz fine channels, providing a total bandwidth of 30.72 MHz. Nine fine channels per coarse channel are always flagged, one central channel and four edge channels on either side to remove aliasing introduced by the polyphase filter bank (Ord et al. 2015). Observations are typically recorded in 112 s "snapshots" with either 0.5 s or 2.0 s integration times. For GLEAM, observations cycle through five frequency bands on a per-snapshot basis, this investigation only considers the three upper frequency bands. For EoR observations, the band is centered on 154 MHz, but the beam-former pointing is regularly adjusted to ensure that the EoR field remains near the center of the field of view.

### 2.1. Primary Beam, Flux Density, and Bandpass Calibration

The visibility data in each snapshot was flagged for radio frequency interference (RFI) using AOFLAGGER (Offringa et al. 2012). A benefit of the radio quiet environment within the MRO is that less than 1% of data is typically flagged as a result of RFI (Offringa et al. 2015).

Calibration was carried out using the real-time calibration and imaging system, referred to as the RTS (Mitchell et al. 2008; Ord et al. 2010), but utilized in an off-line mode to perform an additional polarimetric analysis. For all observations, a pointed scan of 3C444 was used to calibrate the bandpass and to set the absolute flux scale. The flux density of 3C444 at 154 MHz is 81 Jy with a spectral index[28] of $\alpha = -0.88$ (Slee 1977, 1995), tied to the Baars et al. (1977) flux scale. The uncertainty on the absolute calibration is estimated to be better than 10% (Hurley-Walker et al. 2016, in preparation).

For each observing epoch and frequency band, targeted observations of 3C444 were used to measure the direction independent bandpass gains with the RTS, and a polynomial fit was determined for each of the 24 coarse channels. After the bandpass was applied, complex Jones matrices were fitted and the overall solution derived was applied to all visibility data associated with the same observing session, using the calibration scheme described in Section 2.1 of Bernardi et al. (2013). Independent solutions were obtained for each observing session and frequency band. Previous experience has shown that bandpass solutions are stable over an entire night of observing, and so it was assumed that the solutions were not time variable (Bernardi et al. 2013; Hurley-Walker et al. 2014). The relative phase between the instrumental polarizations, i.e.,

---

[27] See http://www.mwatelescope.org/astronomers for a list of currently active observing proposals.

[28] Where $S \propto \nu^\alpha$.
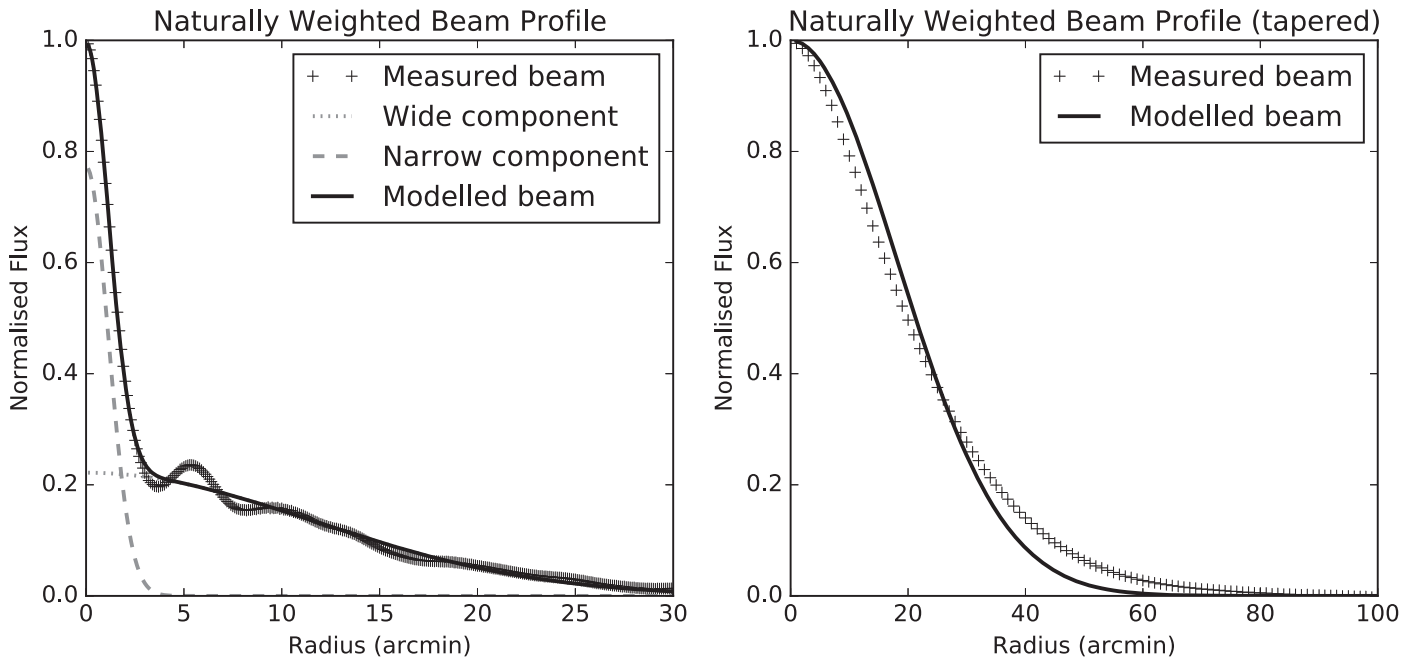
Figure 1. Comparison of naturally weighted synthesized beam without (left) and with (right) (u, v)-tapering. The measured synthesized beam in both instances shows the radially averaged profile of the beam. The untapered beam (left) was modeled with a two-component Gaussian; one corresponding to the narrow component and another corresponding to the wide component. The tapered beam (right) was modeled with a single Gaussian component.

the XY-phase, was not constrained during calibration due to the lack of a bright polarized calibrator in the field. This will result in an excess of leakage from Stokes U into V (Sault et al. 1996); however, based on observations with a 32-tile prototype of the MWA (Bernardi et al. 2013), we estimate that this will result in no more than 20%–30% leakage.

The RTS uses a simple short-dipole analytic model to determine the tile beam used for calibration and imaging. While this is an over-simplification of the true tile beam over the entire frequency range and field of view available to the MWA, it has been shown (Bernardi et al. 2013) that this is sufficient for polarimetric observations below 200 MHz and restricted to fields passing close to or through zenith. To minimize polarization leakage as a result of deviations of the primary beam model from the true beam, only near-zenith observations of the EoR-0 field have been included in this study. Similarly, our investigations primarily use data from the EoR low-band (154 MHz), where the model and true beam match well (Sutinjo et al. 2015). Based on observational tests (Sutinjo et al. 2015), we estimate polarization leakage (primarily Stokes I into Stokes Q) of approximately 1% near zenith and a few percent toward the edge of a typical $25° \times 25°$ field.

2.2. Imaging

Using all available baselines to generate a naturally weighted image results in a point-spread function (PSF) with a narrow 6′ full width at half maximum (FWHM) Gaussian-like peak associated with the longest baselines and a broad ~50′ FWHM Gaussian-like component associated with the dense inner core of the MWA. Figure 1 shows a cut of the naturally weighted MWA beam profile and its decomposition into narrow and broad Gaussian-like components. The RTS does not perform image deconvolution on extended emission during the imaging process and the structured naturally weighted PSF complicates

flux scale measurements of diffuse features. To ensure a near-Gaussian beam and to improve imaging of large-scale features, (u, v) visibilities were tapered with an 82 λ Gaussian taper and baselines above 300λ were excluded. The effect of the tapering can be seen in Figure 1; the resulting naturally weighted PSF is now a single-component near-Gaussian beam with $54′ \times 47′$ FWHM at a position angle of $-1°.8$. This corresponds to a conversion factor of 1 Jy beam^{-1} = 5.6 K at 154 MHz (Wrobel & Walker 1999).

For a 112 s snapshot image using the (u, v)-tapered visibilities, the PSF response in the image plane exhibits two weak (3% level) negative point-like sidelobes ~4° from the peak and a two slightly stronger (10% level) positive point-like sidelobes ~8° from the PSF peak. The sidelobe levels reduce with longer integration times. By avoiding deconvolution, we can minimize processing requirements while only incurring image flux density errors, as a result of non-Gaussian PSF structure, of the order of a few percent. To verify the fidelity of the diffuse structure in the dirty maps, a single EoR snapshot was calibrated and deconvolved using MIRIAD (Sault et al. 1995). The deconvolution process did not greatly affect the diffuse structures in the image and the resulting image was found to be consistent, to within a few percent, with the dirty images generated by the RTS in the zenith region. It should be noted that MIRIAD does not have the capability to calibrate nor correct MWA data for wide-field polarimetric effects and so the results are only valid near zenith. To validate the wider field polarimetric results from the RTS a second independent processing pipeline based on WSCLEAN (Offringa et al. 2014) was used to compare results against. This pipeline also has internal knowledge of the MWA beam and can apply the appropriate corrections for wide-field polarimetry. The output dirty maps from the WSCLEAN pipeline were found to be consistent with the RTS maps over the available field of view and for all four Stokes parameters. Subtle edge differences

Table 2
Summary of Measured Image Noise and Synthesized Beam Characteristics for All Epochs and Imaging Modes

Epoch	Mode	σ_i (Jy beam^{-1})	σ_q (Jy beam^{-1})	σ_u (Jy beam^{-1})	σ_v (Jy beam^{-1})	θ_{maj} (arcmin)	θ_{min} (arcmin)	PA (deg)
1	Diffuse	630	80	102	5.9	54	47	−1.8
1	Point	9.0	3.1	2.4	2.3	2.4	2.2	−47
1	Pulsar	24	1.6	1.5	1.1	4.6	3.8	86
2(a)	Diffuse	690	88	115	39	54	47	−1.8
2(b)	Diffuse	510	240	104	60	48	41	11
2(c)	Diffuse	406	254	140	120	43	37	11
3	Diffuse	600	87	112	6.2	54	47	−1.8
3	Point	11.3	3.0	2.4	2.3	2.4	2.2	−47
3	Pulsar	32	1.4	1.5	1.0	4.1	3.7	−89

Note. The measured image noise for Stokes *I, Q, U,* and *V* are listed under Columns σ_i, σ_q, σ_u, and σ_v, respectively. In all cases, σ_i is dominated by classical confusion and sidelobe confusion. For diffuse imaging modes, σ_q and σ_u are dominated by diffuse polarized structure in the field. θ_{maj} and θ_{min} are the major and minor axes of the synthesized beam (FWHM), respectively. PA is the position angle of the synthesized beam measured from north to east.

were noted, at a level less than 1%, owing to slightly different implementations of the MWA beam model.

Using the RTS, calibrated 25° wide full Stokes (*I, Q, U,* and *V*) dirty image cubes were generated for each snapshot, with 160 kHz frequency channels across the 30.72 MHz band. The images are corrected for dipole projection effects and wide-field effects across the entire field of view during the resampling stage (Ord et al. 2010). A sampling of 3 pixels across the naturally weighted synthesized beam is used in the final imaging. Assuming a receiver temperature of 50 K and a sky temperature of 350 K (Tingay et al. 2013) and taking into consideration the flagging, weighting, and baselines used for imaging, we estimate a theoretical sensitivity of 35 mJy beam^{-1} (1σ) per snapshot over the entire 30.72 MHz band at 154 MHz. When combined with all 44 snapshots in our deepest field (epoch 1), this results in a theoretical sensitivity of 5.3 mJy beam^{-1}. Using the continuum Stokes *V* image of the deepest field as a guide, we measure an actual image rms of 5.9 mJy beam^{-1}. Table 2 summarizes the measured continuum image noise and the synthesized beam parameters for all epochs processed in "diffuse" imaging mode. For total intensity, image rms is dominated by classical confusion and sidelobe confusion (Franzen et al. 2015; Wayth et al. 2015); this is also true for the point-source and pulsar imaging presented below. Similarly, for linear polarization, image rms is limited by diffuse polarized structure within the observed field.

Full Stokes dirty image cubes of the inner 400 square degree region of the field were also produced using uniformly weighted images (the restricted field of view was due to memory limitations encountered when processing a field at increased resolution). The image cubes are considered "dirty" because no deconvolution was performed. All baselines shorter than 50 λ were excluded and no (*u, v*)-tapering was applied. The resulting cubes were better suited for searches of polarized point sources because large-scale emission was effectively filtered out. Table 2 summarizes the measured continuum image noise and the synthesized beam parameters for the two epochs processed in this imaging mode (designated as the "point" mode).

Additional targeted imaging was performed in an attempt to detect a known field pulsar, PSR J2330−2005 (PSR B2327−20), to aid in localizing linearly polarized features. While not ideal, owing to increased sidelobe confusion and PSF structure, natural weighting was used to improve sensitivity. All available baselines were utilized except those

below 100λ; these were excluded to limit confusion and contamination from diffuse emission. Full Stokes dirty image cubes of a 16 square degree region centered on the pulsar ($\alpha = 23^{\mathrm{h}}30^{\mathrm{m}}26\overset{s}{.}885$, $\delta = -20°05'29\overset{''}{.}63$) were produced for epochs 1 and 3. Table 2 summarizes the measured continuum image noise and the synthesized beam parameters for the two epochs processed in this imaging mode (designated as "pulsar" mode).

3. RESULTS

3.1. Total Intensity Continuum Maps

The band-averaged epoch 1 total intensity (Stokes *I*) images optimized for diffuse emission and for point-source analysis are shown in Figure 2. While neither of these images has been deconvolved for the PSF, the beam has been shown to be near-Gaussian and does not significantly degrade the images. To demonstrate that these dirty maps accurately recover diffuse structures, reprocessed 408 MHz Haslam et al. (1982; Rema-zeilles et al. 2015) and 1.4 GHz HIPASS (Calabretta et al. 2014) images of the same region have been included in Figure 2 for comparison. The low level diffuse emission observed in the MWA diffuse map correlates well with diffuse emission seen in the Haslam et al. (1982) 408 MHz data and, while these features are weaker at 1.4 GHz, they are also present in the HIPASS 1.4 GHz data.

3.2. Full Stokes Diffuse Maps

The resulting band-averaged total intensity (Stokes *I*) and linear polarization (Stokes *Q* and *U*) dirty images for the epoch 1 and 3 observations of the EoR-0 field are shown in Figure 3. Because no point-source subtraction or peeling (point-source subtraction with direction-dependent calibration) was performed, the Stokes *I* images are confusion limited and dominated by point sources within the field. Despite the presence of sources with peak brightnesses exceeding 25 Jy beam^{-1} in total intensity, the linear polarization maps contain mostly smooth features and these are uncorrelated with features in Stokes *I*. A few of the brightest sources are just perceptible in the polarization maps at about the 1% level but do not affect the overall structure of the diffuse emission seen in those maps. The *Q* and *U* maps are mostly dominated by smooth extended structures ranging from 1° to 8° in extent and filament-like features, a number of which are approximately
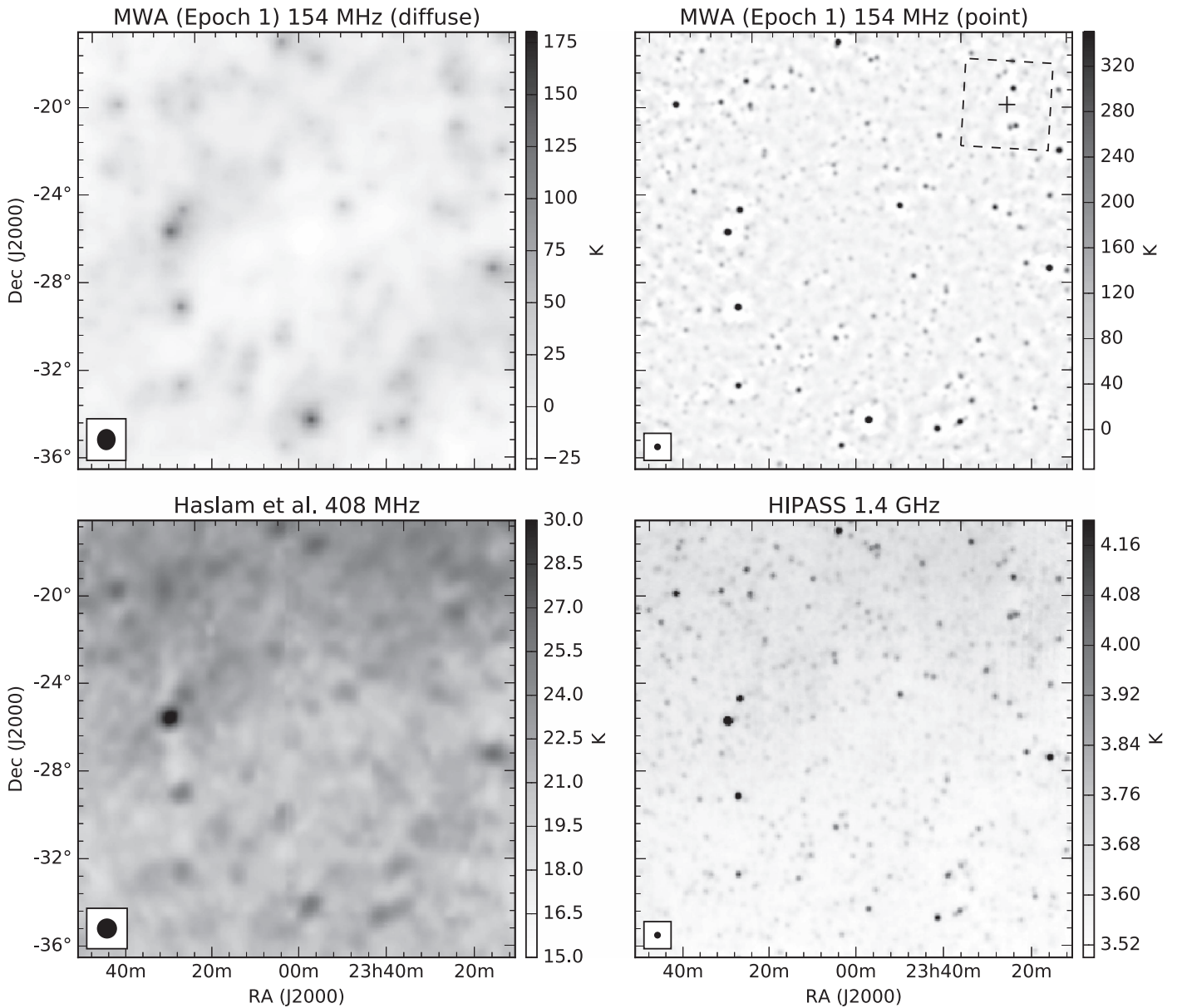
Figure 2. Total intensity maps showing a 20° × 20° portion of the EoR-0 field. The synthesized beam is shown by the ellipse in the bottom-left corner of each map. (Top left) Dirty MWA map at 154 MHz optimized for diffuse imaging (naturally weighted and (u, v)-tapered). The synthesized beam size is 54′ × 47′ FWHM at a position angle of −1°.8. (Top right) Dirty MWA map at 154 MHz optimized for point-source imaging (uniformly weighted with short baseline cut-off applied). The map has been convolved with a 14′.4 FWHM beam to highlight sources. The dashed inset box marks the region imaged in a targeted analysis of PSR J2330–2005; the cross marks the location of the pulsar. (Bottom left) A reprocessed Haslam et al. (1982) 408 MHz map (Remazeilles et al. 2015). Beam FWHM is 51′. (Bottom right) A reprocessed 1.4 GHz HIPASS map (Calabretta et al. 2014). The beam FWHM is 14′.4.

aligned in a northwest direction. Note that while the Stokes I maps are virtually identical in epochs 1 and 3, the Stokes Q and U maps are quite different. In particular, the epoch 3 U image appears to exhibit features found in the epoch 1 Q image and the epoch 3 Q image appears to have inverted features from the epoch 1 U image. The changes observed between the epochs appear consistent with a rotation in the Q–U plane. As will be shown in Section 3.4, these changes are a result of ionospheric Faraday rotation.

For comparison and diagnostic purposes, the band-averaged circular polarization (Stokes V) images and polarized intensity (P) images (formed from the band-averaged Q and U images such that $P = \sqrt{Q^2 + U^2}$) are shown for epochs 1 and 3 in Figure 4. The circular polarization maps clearly exhibit leakage

from Stokes U into Stokes V at the ∼10% level in epoch 1 and the ∼20% level in epoch 3; due to a combination of frequency-dependent XY phase errors that have not been accounted for and uncertainties in the beam model. We note that this is relatively high but even if corrected for, the improvement in Stokes U would only be at a level that is already dominated by existing errors associated with the PSF and sidelobe confusion. We also note that the leakage from Stokes U to Stokes V is not prominent in the uniformly weighted image used for point-source analysis; because the point sources are significantly weaker in Stokes U compared to the diffuse emission and so any leakage would be below the Stokes V noise level.

Comparing the polarized intensity images between epoch 1 and 3, one would expect that the images should remain
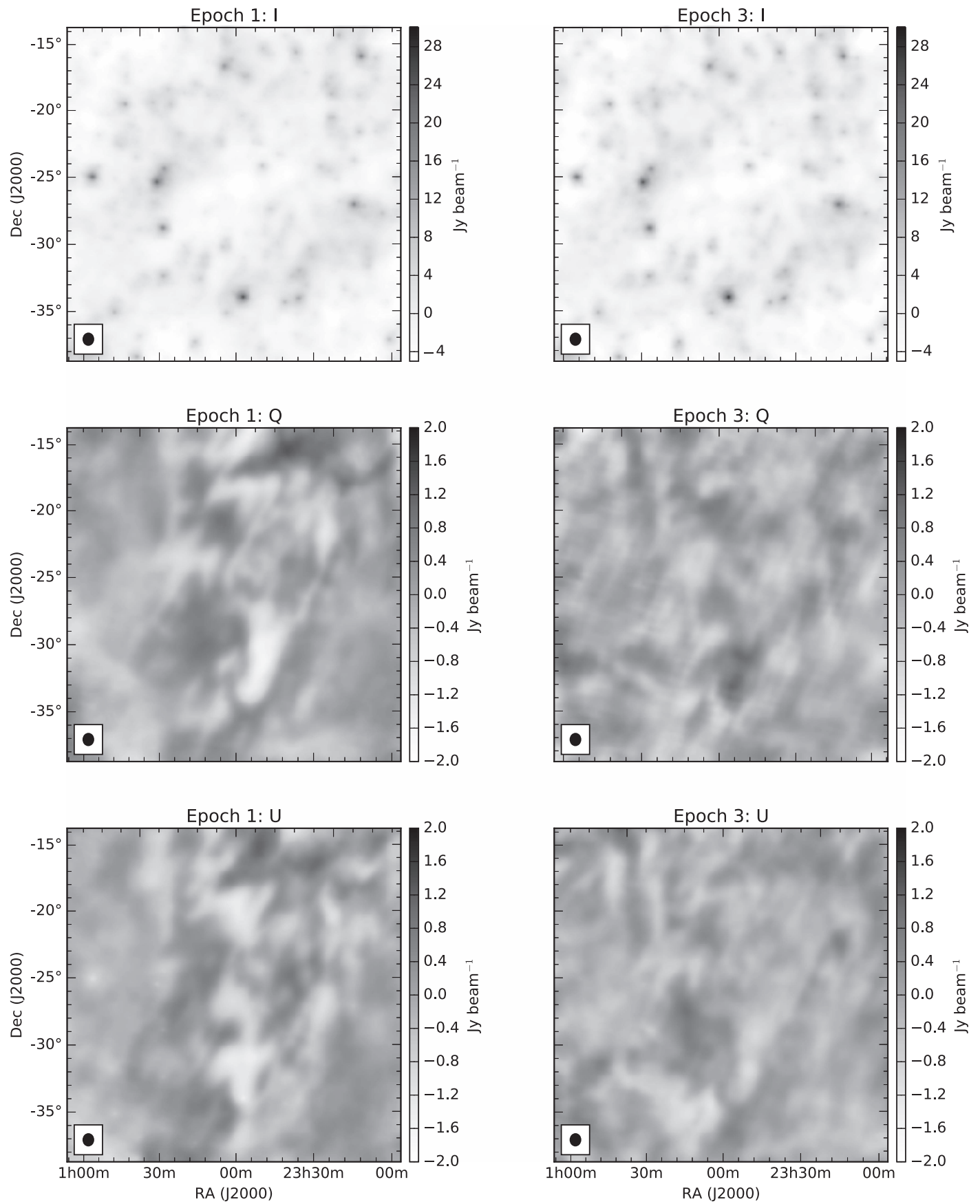
Figure 3. $25° \times 25°$ Stokes I, Q, and U images from deep epoch 1 and epoch 3 data centered on the EoR-0 field. All images are naturally weighted ((u, v)-tapered), band-averaged and dirty (not deconvolved). The synthesized beam size is $54' \times 47'$ FWHM at a position angle of $-1°8$ and is shown by the ellipse in the bottom-left corner of each map. The Stokes I images are highly consistent between epochs but the linear polarization (Stokes Q and Stokes U) is not; this is due to differing ionospheric conditions between the two epochs.
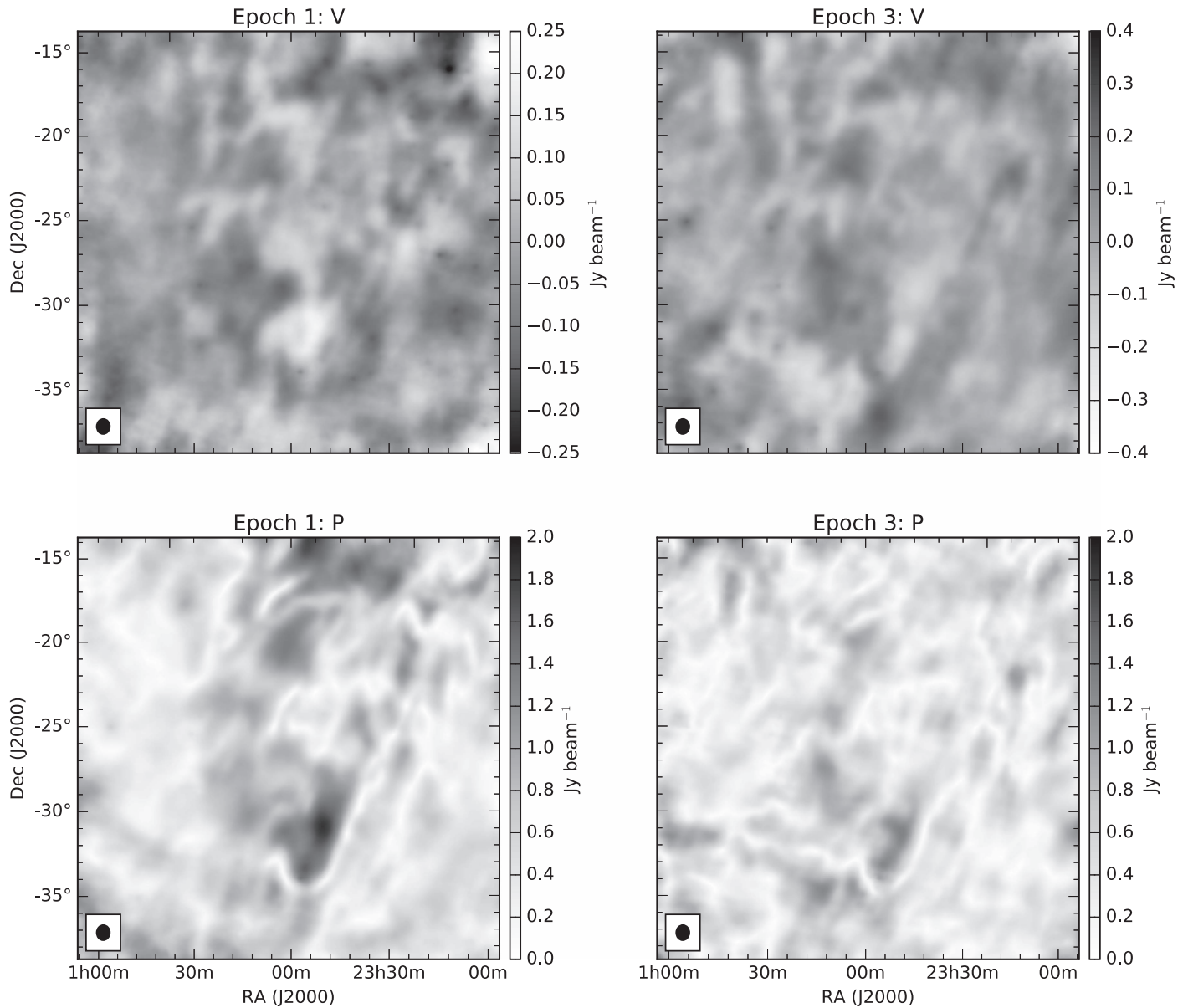
Figure 4. Circular polarization (Stokes *V*) and polarized intensity (*P*) images. Image details are the same as in Figure 3, but the intensity scales of the Stokes *V* images have been adjusted to highlight the leakage seen from Stokes *U*. The polarized intensity images do not show consistent structure as a result of differing ionospheric conditions between the two epochs.

constant between epochs. However, there are clear differences between the two. The epoch 1 image has significantly brighter structures whereas the epoch 3 image does not. These differences are caused by significantly different ionospheric conditions between the two epochs resulting in different levels of depolarization in the band-averaged *Q* and *U* images used to form the polarized intensity images. The polarized intensity image from epoch 1 is dominated by a large ($\sim 4° \times 7°$) and bright feature (peaking at ~ 1.8 Jy beam^{-1}) centered around $\alpha = 23^{\mathrm{h}}50^{\mathrm{m}}$ and $\delta = -31°$. Depolarization canals, unresolved regions with little or no emission in linear polarization, are further clearly visible; many of them laying preferentially in a northwest orientation. The most prominent depolarization canals appear to be associated with the bright extended feature. In particular, one curves around the lower extent of the feature (starting around $\alpha = 0^{\mathrm{h}}$, $\delta = -35°$) and then extends linearly

toward the northwest edge of the field (through $\alpha = 23^{\mathrm{h}}30^{\mathrm{m}}$, $\delta = -25°$).

3.3. RM Synthesis

When propagating through a magnetized plasma, a linearly polarized signal undergoes Faraday rotation. The effect is particularly pronounced at long wavelengths as the magnitude of rotation is proportional to the wavelength squared:

$$\chi(\lambda^2) = \chi_0 + \phi\lambda^2, \tag{1}$$

where $\chi(\lambda^2)$ is the measured linear polarization angle (rad) at wavelength λ (m), χ_0 is the intrinsic polarization angle (rad), and the overall strength of the effect is characterized by the Faraday depth ϕ (rad m^{-2}). The Faraday depth along the

sightline to a source is defined as (Burn 1966)

$$\phi(d) = 0.81 \int_d^0 n_e B_\parallel \cdot dl, \qquad (2)$$

where n_e is the electron density (cm^{-3}) and $B_\parallel$ is the magnetic field component parallel to the line of sight (μG). The integral is performed along the line of sight (of which dl is the differential element) from the observer to a distance d (pc). If Faraday rotation is not taken into consideration at long wavelengths, sources at any appreciable Faraday depth will depolarize over the available observing band, an effect known as bandwidth depolarization.

RM synthesis (Brentjens & de Bruyn 2005) is a technique that takes advantage of the Fourier relationship between the complex polarized intensity as a function of wavelength squared, $P(\lambda^2) = Q(\lambda^2) + iU(\lambda^2)$, and the Faraday dispersion function (FDF) $F(\phi)$, which is the polarized intensity as a function of Faraday depth (Burn 1966), i.e.,

$$P(\lambda^2) = W(\lambda^2) \int_{-\infty}^{+\infty} F(\phi) e^{2i\phi\lambda^2} d\phi, \qquad (3)$$

where $W(\lambda^2)$ is a weighting function and ϕ is the Faraday depth. RM synthesis reconstructs the FDF $F(\phi)$ from an irregularly sampled $P(\lambda^2)$. The rotation measure spread function (RMSF), which is the Faraday depth equivalent of the PSF, is the Fourier transform of the weighting function and depends on bandwidth, channel weighting, and wavelength.

In general, frequency channels may be weighted by $W(\lambda^2)$ to account for varying sensitivity across the band. However, measuring the Q and U image noise in the presence of large-scale structures, which vary dramatically as a function of frequency, is problematic. To simplify processing, we have weighted all frequency channels in the image cubes equally, i.e., $W(\lambda^2) = 1$. We anticipate only a slight loss in overall sensitivity resulting from this choice of weighting scheme because the observed sensitivity across the band is relatively smooth when measured in uniformly weighted images. Using definitions from Brentjens & de Bruyn (2005), for the 154 MHz band with 160 kHz channels, the resulting RMSF provides a resolution of $\delta\phi = 2.3$ rad m^{-2}, maximum-scale-size sensitivity of 1.0 rad m^{-2} and Faraday depth range of $|\phi_{max}| = 160$ rad m^{-2}. Because the maximum-scale size is smaller than the resolution $\delta\phi$, these observations cannot resolve Faraday-thick structures.

The incomplete sampling available in λ^2 results in sidelobes at about the 10% level in the RMSF. These have been accounted for by using the RM clean algorithm, as described by Heald (2009). In summary, the RM clean algorithm deconvolves peaks in Faraday space with the RMSF to determine the location and amplitude of clean components. The resulting clean components are then convolved with a Gaussian restoring function that has an FWHM equivalent to the RMSF resolution (i.e., $\delta\phi = 2.3$ rad m^{-2}).

Figure 5 highlights features observed in Faraday space at three different Faraday depths (+1.0 rad m^{-2}, +3.0 rad m^{-2}, and +7.1 rad m^{-2}) in the epoch 1 data. The vast majority of the diffuse structure appears at low Faraday depths ($\sim$1 rad m^{-2}) and is dominated by a bright extended feature (labelled "Low RM"), which was noted in the epoch 1 polarized intensity map (see Figure 4). Depolarization canals also dominate the entire field-of-view at this Faraday depth

with several of the more significant canals oriented in an approximately SE–NW alignment. At a Faraday depth of +3.0 rad m^{-2}, the bulk of the features seen at +1.0 rad m^{-2} are gone and are replaced by a number of $\sim$2°–4° wide structures in the SE corner of the EoR-0 field (the brightest of which is labelled "Mid RM"). At +7.1 rad m^{-2}, a small, barely resolved, feature is seen to the east (labelled as "High RM"). Just SE of this source is a slightly more extended component that peaks at approximately +9 rad m^{-2}. The mid-to-high RM features may be associated with the increased level of diffuse polarized emission observed by Bernardi et al. (2013) toward the SGP at similar Faraday depths. Figure 6 shows the Faraday depth at peak emission in the Faraday depth cube for each line of sight in the field. The figures show that the majority of the EoR-0 field is dominated by features at low Faraday depths and that these features vary quite smoothly across the field. Apart from the small number of sources already described at higher Faraday depths, there are a number of weak features at negative Faraday depths near the edge of the field; these are not likely to be associated with real features and are caused by a combination of decreased sensitivity at the edge of the field and sidelobe structures contaminating the field at a low signal to noise.

The deconvolved FDFs for the samples taken in the low and high RM regions are shown in Figure 7. The residual rms is 16 mJy beam^{-1} RMSF^{-1}, 42 mJy beam^{-1} RMSF^{-1}, and 29 mJy beam^{-1} RMSF^{-1} for the low, mid, and high RM sources, respectively. The high RM FDF appears to contain more than one peak: a main peak at $\phi = +7.2$ rad m^{-2}, an intermediate 530 mJy beam^{-1} RMSF^{-1} peak at $\phi = +3.5$ rad m^{-2} and a 230 mJy beam^{-1} RMSF^{-1} peak at $\phi = +0.7$ rad m^{-2}. The additional minor peaks in the high RM FDF fluctuate between epoch 1 and 3 and are due to sidelobe contamination, which introduces frequency-dependent structure into the Faraday spectra that is also time dependent.

3.4. RM Distribution and Ionospheric Faraday Rotation

The ionosphere affects observations through positional shifts of background sources and through Faraday rotation of linearly polarized signals. A gradient in total electron content (TEC) of the ionosphere across the field of view will result in positional shifts of sources; this has been observed previously with the MWA and studied in detail (Loi et al. 2015a, 2015b, 2015c). For diffuse polarization, the effect is an order of magnitude smaller than the size of the features being studied and can safely be ignored.

The absolute TEC, in combination with the magnetic field in the direction being observed, can measurably contribute to the observed RM of a background source. The TEC at a given time, from a given location on the Earth, observed toward a particular line of sight, can be estimated based on Global Positioning System models (Arora et al. 2015). Using the TEC estimated by these models in combination with terrestrial magnetic field models, the predicted ionospheric component of Faraday rotation may be determined. An implementation of these models can be found in the ALBUS (Willis et al. 2016) package. We used ALBUS to determine the mean Faraday rotation introduced as a result of the ionosphere during the course of the epoch 1 observation and estimated it to be -0.7 ± 0.2 rad m^{-2}. When corrected for ionospheric Faraday rotation, the distribution of RM in the EoR-0 field peaks at 1.0 rad m^{-2} with a standard deviation of $\sigma_\phi = 0.34$ rad m^{-2};
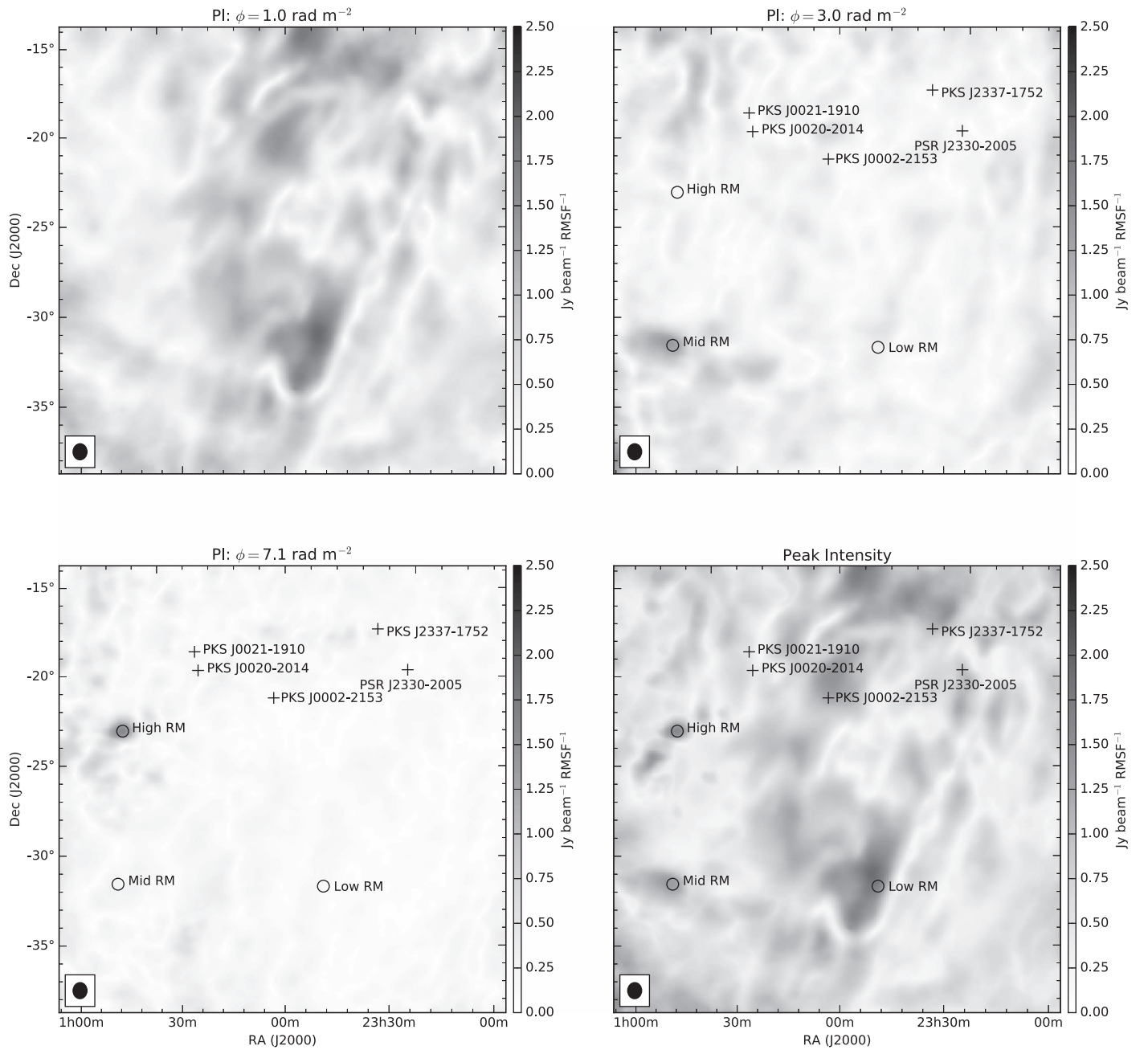
Figure 5. Polarized features observed at three Faraday depths in epoch 1 data taken from the RM cleaned cube (corrected for ionospheric Faraday rotation). The RMSF has an FWHM of 2.3 rad m^{-2}. (Top left) $\phi = +1.0$ rad m^{-2}. (Top right) $\phi = +3.0$ rad m^{-2}. (Bottom left) $\phi = +7.1$ rad m^{-2}. (Bottom right) Peak intensities in the Faraday depth spectra at each spatial pixel. The flux scale is in Jy beam^{-1} RMSF^{-1}. The synthesized beam, shown as a filled ellipse, is $54' \times 47'$ FWHM at a position angle of $-1°.8$. Circles mark the locations of diffuse features referred to in the text. Crosses mark locations of polarized point sources detected in high-resolution imaging; these sources are not visible in the low-resolution images because they are dominated by the presence of large-scale structure.

see Figure 8. A few further sub-peaks are seen within this distribution but the vast majority of features are contained within $-2 < \phi < +10$ rad m^{-2}.

When images are compared across the three epochs at 154 MHz, the total intensity maps remain unchanged. However, there are clear differences in the linear polarization maps, particularly between epoch 1 and the two subsequent epochs. Using RM synthesis and searching for peak emission in Faraday depth for each line of sight revealed that all of the observed structures were consistent between the epochs but that they had been shifted in Faraday space. This is shown in Figure 9 for the epoch 1 and epoch 3 data; here the peak

intensity maps are consistent, but the peak emission occurs at $+0.3$ rad m^{-2} in epoch 1 and at $\phi = -1.2$ rad m^{-2} in epoch 3. Both ALBUS (Willis et al. 2016) and IONFR (Sotomayor-Beltran et al. 2013) predict a shift in the ionospheric component of approximately -1.5 rad m^{-2} in Faraday rotation from epoch 1 to epoch 3 (ionospheric RM of -0.7 rad m^{-2} for epoch 1 and -2.2 rad m^{-2} for epoch 3). When these shifts are applied to the Faraday depth cubes, the peak emission for both epochs occurs at ~ 1.0 rad m^{-2}, verifying that the shift is associated with the ionosphere and not caused by variability or the instrument. The significantly higher Faraday rotation induced by the ionosphere in epoch 3, most likely as a result of a known Coronal Mass
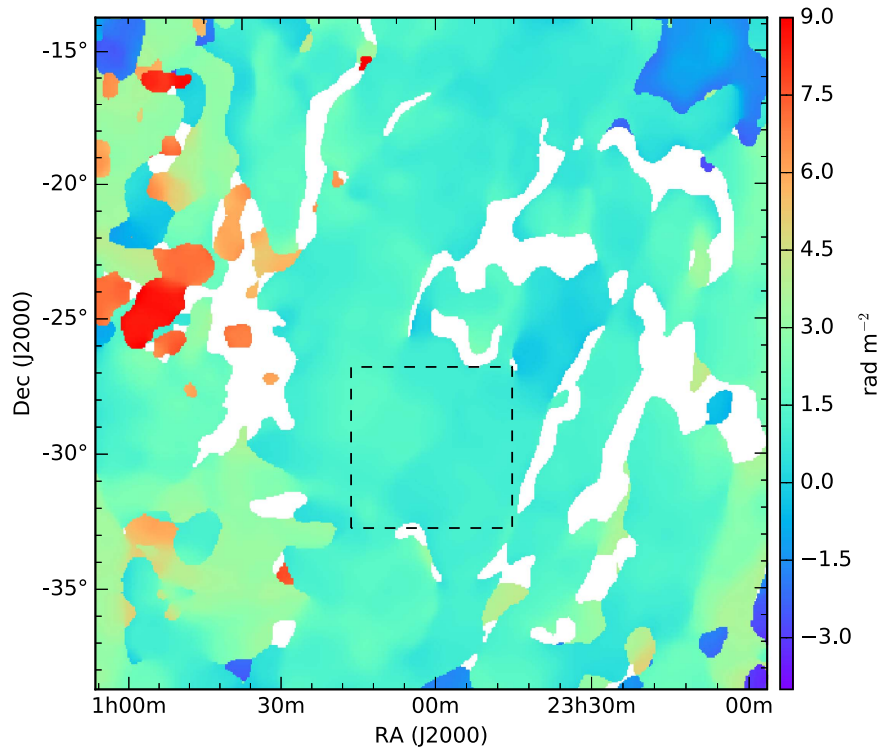
Figure 6. Faraday depth measure at peak polarized intensity for each pixel in the Faraday depth cube (corrected for ionospheric Faraday rotation). Regions with low signal to noise have been blanked out. The Faraday depth is measured in rad m^{-2}. The $6° \times 6°$ dashed square shows the extent of a region containing both smooth Faraday depth variations and high levels of polarized intensity.

Ejection event (Kaplan et al. 2015), also explains the structural differences observed between the two epochs in the band-averaged Q and U images shown in Figure 3. This highlights the need for a correction to mitigate the effects of ionospheric Faraday rotation. However, it also demonstrates that the ionosphere is quite stable as a function of time and direction over the MWA field of view and that, to first order, a single shift in Faraday depth (as opposed to a grid of multiple direction dependent shifts) is sufficient to correct for these ionospheric effects.

An interesting possibility with the MWA, given the high sensitivity to diffuse structures that the instrument provides, is to use the diffuse polarized background to track and measure the influence of ionospheric and heliospheric Faraday rotation. An estimate of the ionosphere-corrected Faraday rotation toward a source of bright diffuse emission (ϕ_{src}) can be determined by performing a least-squares fit that minimizes $\phi_{src} - (\phi_{obs} - \phi_{ALBUS})$ over multiple observing snapshots and/or epochs, where ϕ_{obs} is the observed Faraday rotation toward the source and ϕ_{ALBUS} is the estimated ionospheric Faraday rotation at the time of the observation. By observing over multiple epochs, to overcome the relatively large errors associated with individual predictions of ϕ_{ALBUS}, the overall error in ϕ_{src} can be minimized. Once an estimate of the ionosphere-corrected Faraday rotation is established, it can be used to estimate the ionospheric component of Faraday rotation at that source location at any epoch. Using this approach for all available snapshots in each of the three epochs, the fit to ϕ_{src} of the high RM source (see Figure 5) was determined to be $\phi_{src} = 7.20 \pm 0.01$ rad m^{-2}. Figure 10 plots the ionospheric component ($\phi_{obs} - \phi_{src}$) at the high RM source location for each snapshot and epoch. The measured component tracks both predictive models quite well from epoch to epoch and even

from snapshot to snapshot. This demonstrates that observations of diffuse polarization may allow the effects of the ionosphere to effectively be calibrated in fields where the RM structure has been previously determined, without the need to resort to predictive models. The technique also has the potential to aid ionospheric studies by mapping ionospheric changes both temporally and spatially over a wide field of view. In combination with predictive models, this technique may also provide a means to detect and track the propagation of space weather events, as caused by coronal mass ejections or solar flares, by observing the shift they impart on the RM signature of the diffuse polarized background (Oberoi & Kasper 2004).

3.5. Gradient Maps

To examine filamentary magnetized structures believed to result from turbulence in the local ISM Burkhart et al. (2012), polarization gradient maps of the Stokes vector (Q and U) were formed using the method described by Gaensler et al. (2011). The polarization gradient function is defined as

$$|\nabla P| = \sqrt{\left(\frac{\partial Q}{\partial x}\right)^2 + \left(\frac{\partial U}{\partial x}\right)^2 + \left(\frac{\partial Q}{\partial y}\right)^2 + \left(\frac{\partial U}{\partial y}\right)^2}. \quad (4)$$

Time-dependent effects were examined by comparing changes in the gradient map from snapshot to snapshot and against the time-averaged data set. Figure 11 shows gradient maps from the epoch 1 observation using a single 112 s snapshot compared against a gradient map using all of the available data from that epoch. When corrected for ionospheric effects, the structures seen in these gradient maps are centered at a Faraday depth of $+1.0$ rad m^{-2} as this is where the bulk of the polarized emission exists (see Figure 8).
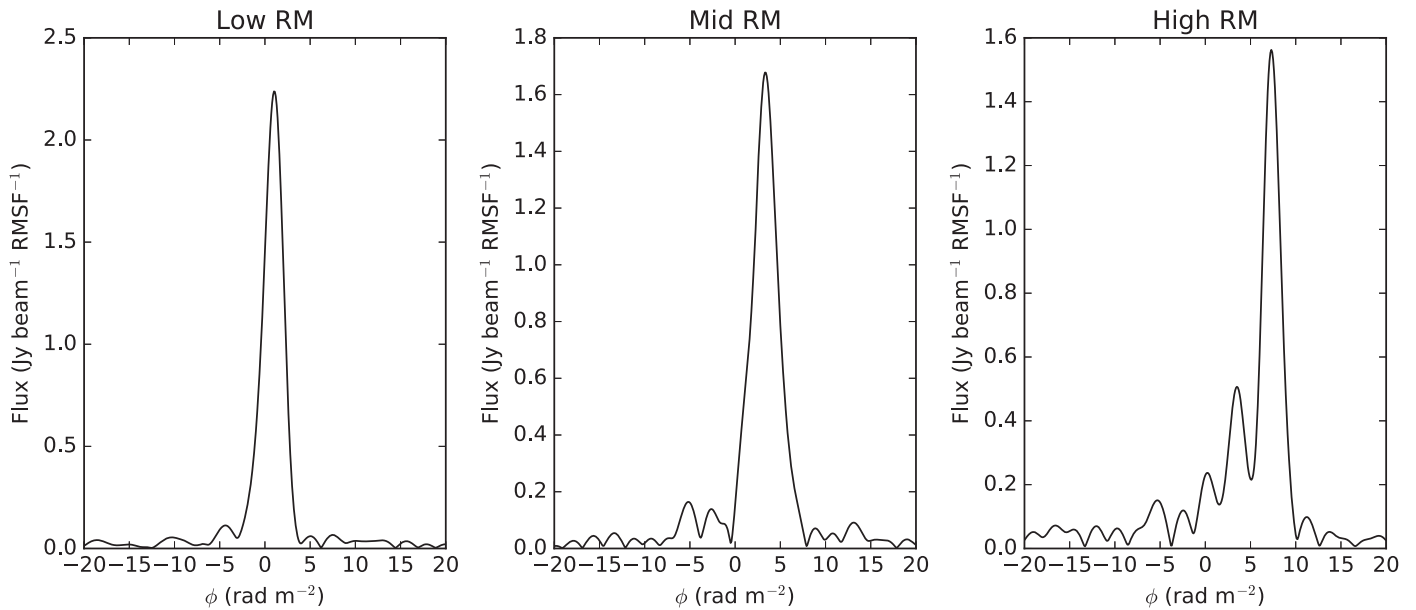
Figure 7. Sample Faraday dispersion functions (corrected for ionospheric Faraday rotation) shown for the low ($\phi = +1.0$ rad m^{-2}), medium ($\phi = +3.0$ rad m^{-2}), and high ($\phi = +7.1$ rad m^{-2}) RM features highlighted in Figure 5. The three Faraday dispersion functions shown here correspond to the three peaks visible in the RM distribution plot shown in Figure 8. No features above the noise floor are seen outside of the Faraday range shown here. The Faraday dispersion functions were deconvolved with RMCLEAN (Heald 2009).

The most prominent features in Figure 11 remain stable as a function of time. Minor changes can be seen in the fainter structures and these are primarily due to a combination of image noise, sidelobe confusion, and errors associated with incomplete (u, v) sampling. We note that the first few snapshots of epoch 1 are detrimentally affected by the presence of the Galactic plane within a far sidelobe because this epoch included low elevation beam-former pointings that were not used in the epoch 2 or epoch 3 data. The projected baselines of the MWA are severely foreshortened for sources at low elevation and the array is particularly sensitive to bright and extended sources in those locations (Thyagarajan et al. 2015). Nonetheless, when integrating data over a wide range of hour angles, the source sidelobe effects are diluted and the exclusion of the affected snapshots has a minimal impact on the final integrated gradient map. Gradient maps were also produced for the remaining epochs at 154 MHz, but no significant changes were observed once the maps were corrected for ionospheric Faraday rotation.

To examine the evolution of gradient map features as a function of observing frequency, gradient maps were created for the three GLEAM bands, i.e., epochs 2(a), 2(b), and 2(c). The EoR-0 field was only fully visible in the first snapshot of the epoch 2 data because the Sun was in the process of setting just as the field was passing through zenith. As such, the sensitivity is limited to that of a single snapshot in these data. Figure 12 shows the resulting gradient maps for each band of epoch 2 data, with channels across each 30.72 MHz band averaged to increase the signal to noise. The point-like sources that begin to appear in epoch 2(b) and dominate in epoch 2(c), result from apparent polarization leakage from bright Stokes I sources. The level of leakage increases with frequency and angular distance from zenith. For the most part, this leakage is due to errors in the primary beam model and will be reduced once improved beam models are implemented into the imaging pipeline (Sutinjo et al. 2015). The leakage in epoch 2(a) is minimal because this is where the beam model and instrument

were designed to perform optimally; thus, its behavior is well-defined. Increased noise levels are also evident at the edge of the field in the higher frequency bands as a result of the decreased field of view available in those bands.

Comparing the gradient maps in the three different bands, the dominant features are stationary with respect to spatial coordinates in the epoch 2(a) and 2(b) images. Some features, such as the linear feature that runs from NW to SE near the western edge, remain persistent over all three of the bands. The weaker structures are more difficult to trace, particularly in epoch 2(c), as a result of the poor sensitivity available in a single snapshot and systematic issues associated with the beam, noise, and available field of view.

An alternative view of the frequency-dependent behavior of the polarized gradients in the field can be obtained from the deep epoch 1 EoR-0 observations, albeit over the limited range of frequencies available in that observation (138.88–169.60 MHz). The epoch 1 data provide sufficient sensitivity, as a result of the longer tracking observation available, to study the polarization gradient evolution on a per-160 kHz channel basis. Figure 13 presents an animation of the gradient map as a function of frequency across the 30.72 MHz band of the 154 MHz epoch 1 observations; in this animation, subsets of 6×160 kHz channels have been frequency-averaged to form a smaller number of 1.28 MHz channels. The polarized gradients are now more prominent in each of the frequency channels and can be seen to vary smoothly in intensity as a function of frequency but show no significant spatial movement. In general, once features appear at lower frequencies, they continue to persist up to the higher frequency gradient maps. For example, the gradient around the bright polarized feature labelled "Low RM" in Figure 5 persists over the entire band. However, SE to NW gradients appear toward the east and west only in the upper portion of the band. Similarly, features in the northern part of the image, some forming loop-like structures, also only appear in the upper end of the band.
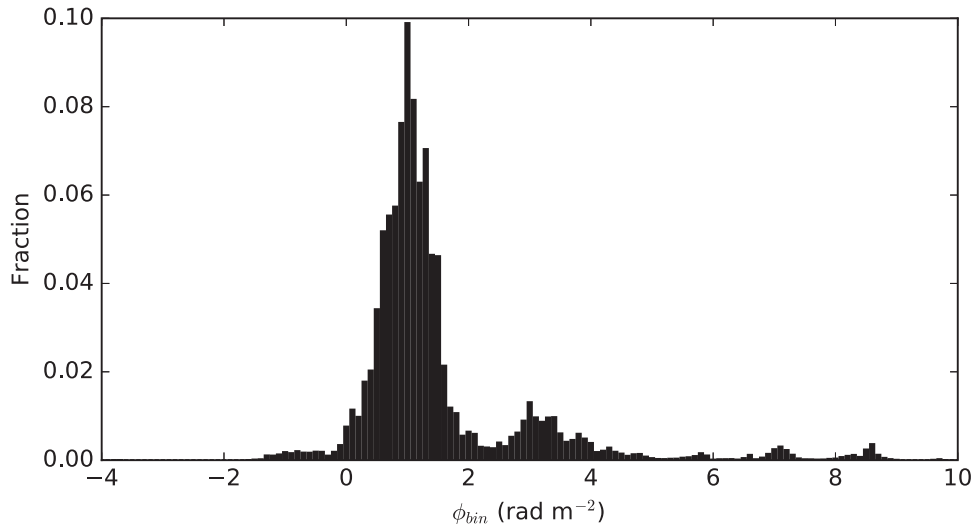
Figure 8. Distribution of rotation measures in the EoR-0 field after ionospheric correction and performing RMCLEAN to remove sidelobes in Faraday space. The binning width is 0.1 rad m^{-2}. The main peak of the distribution is at 1.0 rad m^{-2}. Sub-peaks in the distribution are due to features present at higher Faraday depths.

3.6. Polarized Point Sources

The uniformly weighted polarization image cubes generated using all of the longest MWA baselines are well suited for the detection of polarized point sources. An initial inspection of the RM cube, created using the uniformly weighted Stokes Q and U cubes, reveals a clear detection of the extragalactic source PKS J0021–1910 (PKS B0018–194). A cut-out image for the source and its associated FDF are shown in Figures 14 and 15, respectively. In the uncorrected epoch 3 data, the source has an RM of +5.6 rad m^{-2} and is detected with a signal to noise of 10 in each snapshot. When corrected for ionospheric effects using ALBUS predictions of the ionospheric Faraday rotation, a fit of $\phi = +7.8 \pm 0.1$ rad m^{-2} is obtained for this source. With a total intensity of 4.7 Jy beam^{-1} and a polarized intensity of 140 mJy beam^{-1}, the source is 3.0% polarized. The polarimetric characteristics of the source are consistent with a measurement made at 1.4 GHz, RM = 3.6 ± 5.2 rad m^{-2} and 3.67% polarization (Taylor et al. 2009).

A subsequent search was performed concentrating on the locations of known polarized sources, using the Taylor et al. (2009) catalog as a reference. The catalog contains 399 polarized sources within the 400 sq. degree region imaged around the EoR-0 field. We use a conservative 14σ cut-off in the time-averaged data cube to ensure that spurious detections are not made as a result of polarization leakage from bright Stokes I sources and the associated sidelobe structure this leakage introduces into the Faraday spectra. Any sources with $|RM| < 1$ rad m^{-2} were also filtered out because these would most likely trigger false-positives as a result of polarization leakage. In all, two sources were detected: PKS 0002–2153 (PKS B2359–221) and PKS J0021–1910 (PKS B0018–194). The FDFs for these sources are shown in Figure 15.

Since deep observations were made at two epochs, a further test of the sources was made by checking whether their RMs were shifted in Faraday space by an amount that was consistent with the expected shift caused by the different ionospheric conditions between the two epochs. The advantage of this method is that it can identify real sources that were confused with instrumental leakage, because in at least one of the epochs, such a source would be shifted sufficiently away from RM =

0.0 rad m^{-2} to allow a positive identification. All of the previously detected sources were verified using this method and two additional sources were also identified: PKS J2337–1752 (PKS B2335–181) and PKS J0020–2014 (PKS B0017–205). Figures 16(a) and (c) show the RM synthesis components detected in epochs 1 and 3. In epoch 1 the instrumental component and the source components are confused near RM = 0.0 rad m^{-2} for both PKS J0020–2014 and PKS J2337–1752. In epoch 3, the ionosphere clearly shifts the source RM away from the instrumental component, thus enabling a positive identification. The FDFs for these two sources are shown in Figure 16.

The parameters associated with all detected point sources are summarized in Table 3. All but PKS J2337–1752 have RMs consistent with those measured by Taylor et al. (2009). Not all of the sources appear to have been significantly depolarized at MWA wavelengths compared to observations at 1.4 GHz, which suggests that there is not a systematic reason to explain the overall small number of detections. The two most highly polarized extragalactic sources, PKS J0020–2014 and PKS J0021–1910, are also the two largest sources in spatial extent among our detected sources. PKS J0020–2014 is a giant radio galaxy with a redshift of $z = 0.197$ (Ishwara-Chandra & Saikia 1999) and an extent of 1.22 Mpc, while PKS J0021–1910 is a known double radio source with a redshift of $z = 0.0952$ and an extent of 270 kpc (Reid et al. 1999).[29] The remaining sources are all relatively compact.

The pulsar PSR J2330–2005 does not appear in the Taylor et al. (2009) catalog and is not detected in the uniformly weighted MWA data. It is, however, detected in both circular and linear polarization and in both epochs in the targeted search, using naturally weighted data with short baselines removed (to avoid confusion from the diffuse structures). The parameters associated with the pulsar are summarized in Table 3 and the FDF is shown in Figure 17. The secondary peaks in the FDF for the pulsar are unlikely to be real—most likely they are due to a combination of thermal noise and

---

[29] Assuming a spatially flat ΛCDM cosmology with matter density $\Omega_M = 0.286$, vacuum energy density $\Omega_\Lambda = 0.714$, and Hubble constant $H_0 = 69.6$ km s^{-1} Mpc^{-1} (Wright 2006).

13
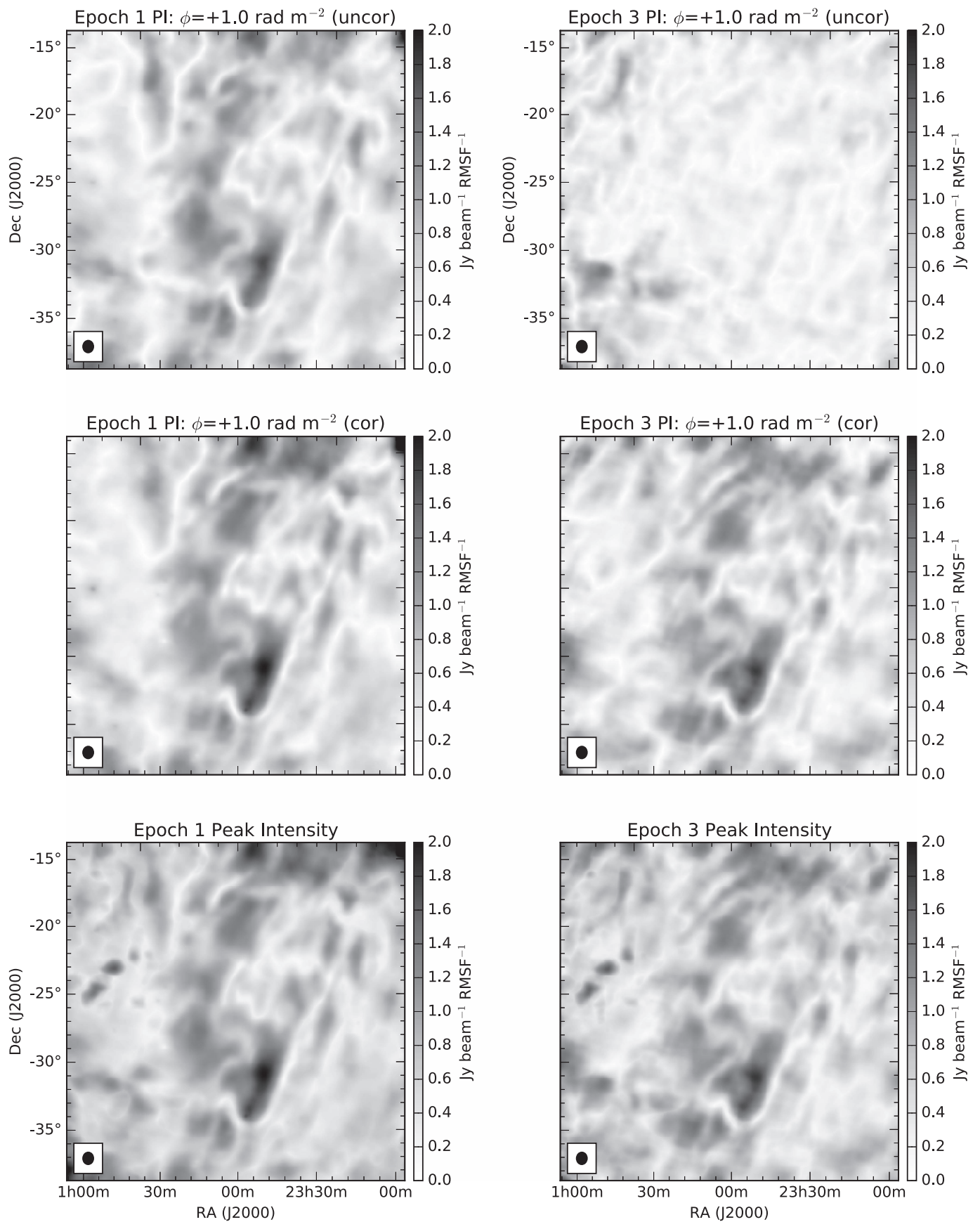
Figure 9. Effect of ionospheric Faraday rotation on diffuse polarization as observed in epochs 1 and 3. Top: polarized intensity at $\phi = +1.0$ rad m^{-2} before correcting for ionospheric Faraday rotation. Center: polarized intensity at $\phi = +1.0$ rad m^{-2} after correcting for ionospheric Faraday rotation. Bottom: peak intensity in the Faraday spectra at each spatial pixel. ALBUS reports an ionospheric Faraday rotation of -0.7 rad m^{-2} in epoch 1 and -2.2 rad m^{-2} in epoch 3. Differences observed near the edge of the field between the two epochs after ionospheric correction are due to primary beam errors and sidelobe confusion.
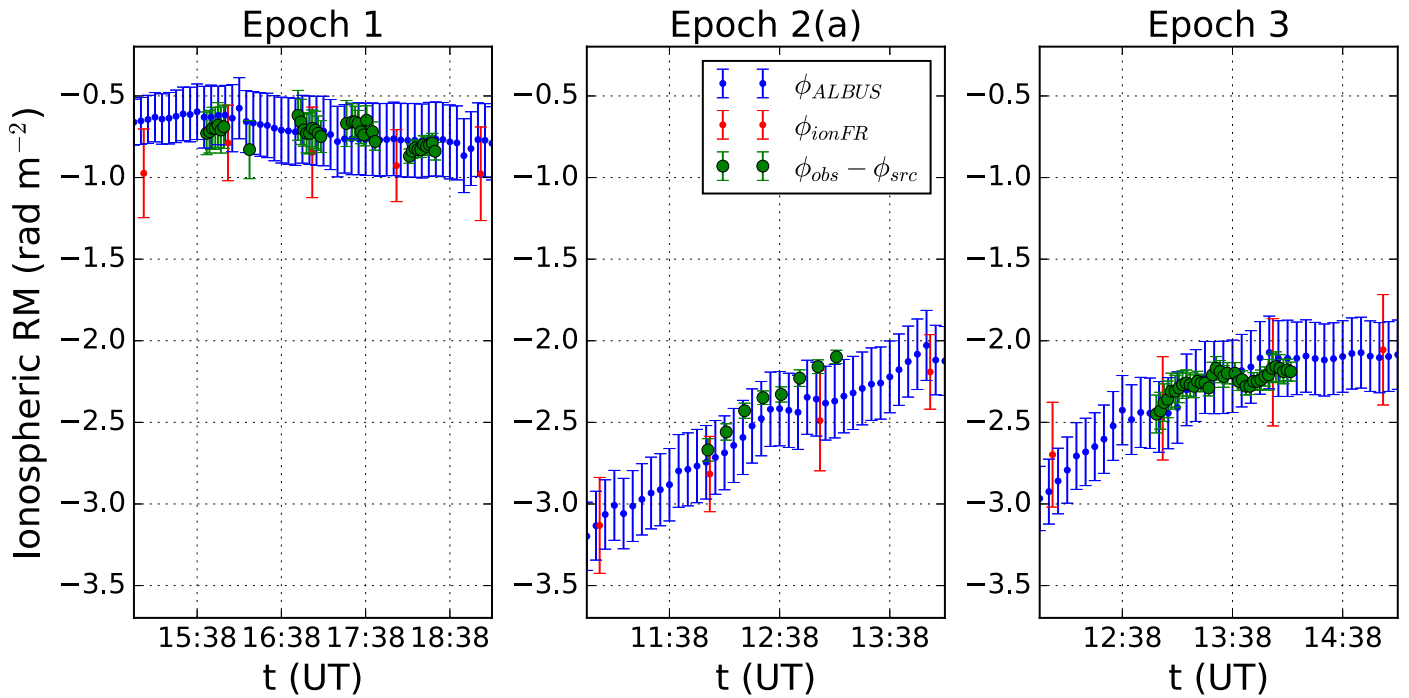
Figure 10. Measurements of ionospheric Faraday rotation (ϕ_{obs} is the observed Faraday rotation of a source and ϕ_{src} is the previously determined ionosphere-corrected Faraday rotation of the source) at the position of the high RM feature shown in Figure 5 for each observed snapshot and epoch (green points). The blue and red points are the predicted components of ionospheric Faraday rotation from ALBUS (ϕ_{ALBUS}) and IONFR (ϕ_{ionFR}), respectively. Note that an additional seven 2 minute snapshots from epoch 2(a) were used here to track the high RM feature as it drifted through the zenith-pointed beam of that observation; however, those snapshots were not used in subsequent processing because the bulk of the EoR-0 field had already drifted out of the field of view.

sidelobe noise as a result of the complicated PSF beam shape that results from natural weighting. In circular polarization, we measure a total flux density for the pulsar at 154 MHz of 8.9 ± 1.1 mJy in epoch 1 and 9.6 ± 1.0 mJy in epoch 3. We estimate a fractional circular polarization of ∼7% based on the total intensity of 140 mJy measured at the pulsar position; however, the field is highly confused in total intensity at this level. As such, the total intensity is most likely over-estimated and the fractional polarization is thus a lower limit. This would be consistent with the 22% circular polarization observed in the integrated pulse profile of the pulsar at 648 MHz (McCulloch et al. 1978).

Offringa et al. (2016) performed a deep point-source survey of the EoR-0 field using 45 hr of MWA data and achieved a sensitivity of 0.6 mJy beam^{-1} in polarization. Using a novel peeling algorithm, spectra for the 586 brightest sources in the field were presented. Unfortunately, PKS J0020–0014 is a resolved source and so was discarded from the catalog and PSR J2330–2005 fell outside of the restricted field of view of the survey. PKS J0021–1910 appears in the catalog but is not detected in polarization. The Offringa et al. (2016) survey did not consider Faraday rotation of the source and so linearly polarized sources with non-zero RM are depolarized. In addition, when combining results from multiple epochs, ionospheric Faraday rotation was also not considered; this too would lead to depolarization of linearly polarized sources (a similar issue was encountered by Moore et al. 2016 in PAPER observations). It is thus not surprising that linearly polarized sources were not detected by Offringa et al. (2016), but circularly polarized sources should not be as greatly affected when combining data from multiple epochs. Indeed, on closer inspection, PSR J2330–2005 is detected in the Offringa et al. (2016) data at the 6.3% level with

a circularly polarized flux density of 6.5 mJy (A.R. Offringa 2016, private communication).

4. DISCUSSION

4.1. Size-scale of Structures in Linearly Polarized Emission

The linearly polarized features seen in Figure 3 are highly prominent even in single 112 s snapshot images. LOFAR observes similar features at 160 MHz in long (∼6 hr), high resolution (∼3′–4′), and sensitive (∼70–300 μJy PSF^{-1}) observations (Jelić et al. 2014) of the ELAIS-N1 field ($l = 84°$, $b = +45°$) and Jelić et al. (2015) observations of the 3C196 field ($l = 171°$, $b = +33°$) but at significantly lower signal to noise. The LOFAR observations differ from the MWA observations in that they incorporate longer baselines, are at lower Galactic latitudes, and their imaging utilizes a robust image weighting of zero, which results in higher resolution (∼3′–4′) images compared to the ∼50′ naturally weighted and (u, v)-tapered images of the MWA presented here. Factoring in the beam size, the Jelić et al. (2014) LOFAR observations have a sensitivity of ∼650 mK at the ∼4′ scale, whereas the MWA epoch 1 observations have a sensitivity of ∼33 mK at the ∼50′ scale.

The unique baseline distribution and radio quiet location of the MRO (Offringa et al. 2015) give excellent sensitivity to structures of $1°$–$10°$ in extent and sample a region not accessible to other low-frequency instruments such as LOFAR (van Haarlem et al. 2013), for example. While the 128 tiles of the MWA provide a total of 8128 baselines out to almost 3 km, the peak sensitivity of the array is derived from its dense inner core, which was specifically designed for EoR science. Figure 18 shows the fraction of baselines as a function of baseline length. Approximately 8.5% of the available baselines
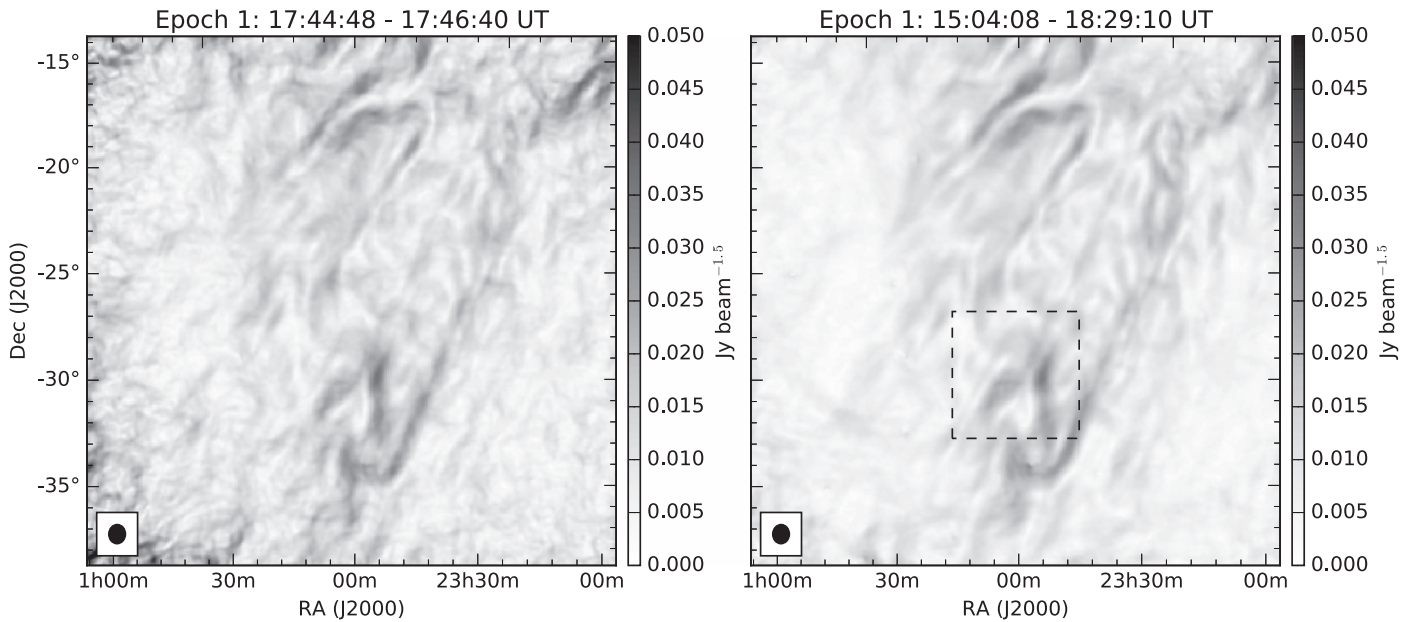
Figure 11. Left: an ionosphere-corrected polarization gradient map from a single 112 s snapshot of epoch 1 data. Right: the ionosphere-corrected polarization gradient map derived from time-averaged epoch 1 data (44×112 s snapshots). Units are in Jy beam$^{-1.5}$. The $6° \times 6°$ dashed square shows the extent of a region containing both smooth Faraday depth variations and high levels of polarized intensity.

(689) are shorter than 60 m and nearly 15% (1183) are shorter than 120 m. The combination of sensitivity to large-scale structure and the relatively large (u, v)-tapered naturally weighted beam explain why the observed polarized features are so much brighter in the MWA images. In addition to providing increased sensitivity, the large number of short baselines also provide excellent snapshot imaging capabilities. This enables variations in ionospheric Faraday rotation to be monitored and calibrated for on short timescales. Although not utilized here, it is possible that observations of the linearly polarized emission may also be used to constrain XY-phase during the calibration phase; thus reducing the effect of leakage from Stokes U into Stokes V.

Ultimately, the Amsterdam-ASTRON Radio Transients Facility and Analysis Center (Prasad et al. 2014) should provide LOFAR with short baseline imaging capability. Similarly, the LWA (Long Wavelength Array, Ellingson et al. 2009) has a compact baseline configuration; however, it operates at longer wavelengths compared to the MWA and will be more greatly affected by the ionosphere.

The single-dish observations of Vinyaikin & Paseka (2015) at low frequencies (151.5–290 MHz) over a number of selected regions of the sky also detected the presence of 5°–10° features in linear polarization. They suggested that these features would be undetectable by interferometric observations because of the lack of short-spacings. However, despite being an interferometer, the MWA provides sensitivity to these scale sizes and thus bridges the gap between traditional single-dish and interferometric observations.

4.2. The Nature of Diffuse Polarization

A feature of the observed linear polarization is the lack of correlation with the Stokes I map at 154 MHz (see Figure 3). The stark difference between features in linear polarization and total intensity has been noted at other wavelengths, e.g., Wieringa et al. (1993) at 325 MHz; Haverkorn et al. (2003b) at

350 MHz; Bernardi et al. (2013) at 189 MHz; Gray et al. (1998) and Gaensler et al. (2011) at 1.4 GHz; and Sun et al. (2014) at 2.3 and 4.8 GHz. The prevailing interpretation is that the ionized foreground gas modulates small-scale RM structures onto an intrinsically highly polarized smooth synchrotron background via Faraday rotation.

The observed linearly polarized emission at 154 MHz is restricted to low Faraday depths ranging from $\phi = -2$ to $9 \, \mathrm{rad \, m^{-2}}$ (see Figure 8), with no other significant emission seen out to $|\phi_{\mathrm{max}}| = 160 \, \mathrm{rad \, m^{-2}}$. The distribution in RM is similar to that observed with the 32-tile MWA prototype (Bernardi et al. 2013) at 189 MHz in a larger region that includes the EoR-0 field, and to LOFAR observations at 150 MHz in the ELAIS-N1 (Jelić et al. 2014) and 3C196 fields (Jelić et al. 2015).

The mean brightness temperature of the linearly polarized emission observed with the MWA at 154 MHz is ~1.8 K in the east (toward the SGP) for the band-averaged data, but increases toward the center of the EoR-0 field to a mean brightness temperature of ~4 K and a peak of 11 K. Increased levels of polarized emission were observed in this region by Bernardi et al. (2013) at 189 MHz with 15′.6 resolution using the 32-tile prototype of the MWA, with peaks up to 13 K. Similarly, observations by Mathewson & Milne (1965) at 408 MHz with 48′ resolution and Wolleben et al. (2006) at 1.4 GHz with 30′ resolution also suggest higher than ambient levels of polarized emission in this region. The emission appears to be coincident with part of a polarized structure identified by Wolleben (2007), which may be associated with the southern extension of the North Polar Spur. However, as noted by Bernardi et al. (2013), there is little correspondence in detailed structure of the linearly polarized maps seen at MWA wavelengths and those at either 408 MHz and 1.4 GHz.

Diffuse emission in total intensity is weak in the EoR-0 field and difficult to separate from bright confusing sources that are within the field; a significant fraction of the diffuse emission may exist at spatial scales to which the MWA is not sensitive.

16
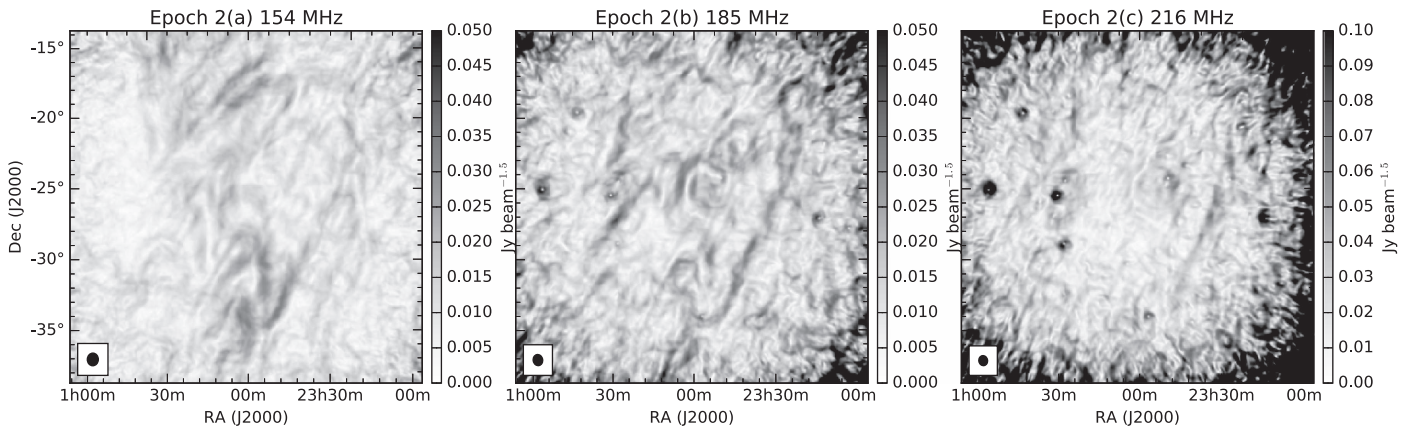
Figure 12. Gradient maps from ionosphere-corrected epoch 2 data of the EoR-0 field in three available frequency bands: 154 MHz (left), 185 MHz (center), and 216 MHz (right). Clear evidence of polarization leakage, primarily contamination from Stokes *I* point sources, is seen in the higher frequency bands where beam model errors are more apparent. The available field of view also decreases as a function of increasing frequency and so the higher frequency maps exhibit increased levels of noise at the edge of the field.

However, an estimate of fractional polarization can be obtained by extrapolating total intensity measurements from higher frequency observations. At 408 MHz (Mathewson & Milne 1965), the total intensity flux is 19.5 ± 2 K, the measured polarized flux is ~3–4 K (15%–21% polarized), and the temperature spectral index[30] for the total intensity emission around the SGP (Guzmán et al. 2011) is $\beta = 2.55$ ($\alpha = -0.55$). Extrapolating to 154 MHz, the total intensity is estimated to be ~246 K. We observe ~4 K polarization at 154 MHz, which corresponds to 1.6% fractional polarization and a peak of 11 K (~4.5% fractional polarization). This is significantly lower than the fractional polarization at 408 MHz, but is in line with the 1.5% fractional polarization seen with LOFAR at 150 MHz in the ELAIS-N1 field (Jelić et al. 2014).

4.3. Localization of Polarized Emission

An estimate of the distance to the polarized emission can be determined by comparing the RM of the emission against the overall contribution to RM of the Galaxy in the direction of the field. In the direction of the brightest features in the polarized intensity map, we measure a typical ionosphere-corrected RM of $+1.0 \pm 0.3$ rad m^{-2} (see Figure 8). Estimates of the full Galactic contribution to RM in this same region, based on measurements of extragalactic Faraday rotation (Oppermann et al. 2015), result in an RM of $+9.0 \pm 1.6$ rad m^{-2}. If the thermal electron density in the Milky Way is assumed to be an exponential disk with a mid-plane free electron density $n_{e,0}$ (cm^{-3}) with a scale height H and a uniform vertical magnetic field B_z (μG), then the expected RM (rad m^{-2}) out to a distance z (pc) is (Mao et al. 2010)

$$\text{RM} = 0.812 B_z n_{e,0} H (1 - e^{-z/H}). \qquad (5)$$

Using the measured RM at extragalactic distances, $+9.0 \pm 1.6$ rad m^{-2}, we can estimate the conditions of the magnetized plasma in the direction of the EoR-0 field as a function of the scale height H. Solving for z, using the measured RM of the observed diffuse emission ($+1.0 \pm 0.3$ rad m^{-2}), we estimate the distance to this emission is $z \sim (0.12 \pm 0.04) H$. Estimates of the scale height toward

the SGP, which is effectively the thick-disk component of the Milky Way, range between 930 pc (Berkhuijsen et al. 2006) and 1830 pc (Gaensler et al. 2008); this corresponds to a distance of ~110–220 pc to the polarized features. There are a significant number of assumptions and uncertainties associated with this estimate, but it is sufficient to determine that the source of the polarized emission is in the local region of the Galaxy. The structures may even be constrained to lie within the local bubble, which extends out to 50–200 pc from the Sun but is elongated toward high southern Galactic latitudes (Lallement et al. 2003).

A more significant effect that may be used to localize the features with improved precision is that of depolarization. There are three prominent effects that can cause depolarization at long wavelengths: bandwidth, beam, and depth depolarization. Bandwidth depolarization occurs when there is a significant rotation of the polarization angle across a single spectral channel. Beam depolarization is caused by fluctuations in polarization angle across the synthesized beam. Depth depolarization is caused by fluctuations in polarization angle along the line of sight. For the MWA, bandwidth depolarization is negligible for Faraday depths out to $|\phi_{\max}| = 160$ rad m^{-2} (see Section 3.3). The combined effects of depth depolarization and beam depolarization limit our ability to detect polarized emission beyond a certain distance, known as the polarization horizon (Landecker et al. 2002). The polarization horizon depends on frequency, synthesized beam width, and physical properties of the medium in the observing direction (due to variations in the magnetic field and length-scale density along different lines of sight).

At 1.4 GHz, the polarization horizon is typically of the order of thousands of parsecs, e.g., Gaensler et al. (2001), whereas at 408 MHz this reduces to ~150 pc (Mathewson & Milne 1965). At 154 MHz with the MWA, beam depolarization is a major concern owing to the large PSF of the observations presented here. However, LOFAR observations at significantly higher resolution observe levels of fractional polarization (Jelić et al. 2014) similar to that seen with the MWA. Depth depolarization is also a significant effect that will limit our long wavelength observations to structures that are relatively local compared to higher frequency observations because more distant structures are significantly depolarized by the foreground ISM. Assuming depth depolarization is the dominant factor and assuming

---

[30] $T \propto \nu^{-\beta}$ and $\alpha = 2 - \beta$; where T is the brightness temperature, ν is the observing frequency, β is the temperature spectral index and α is the spectral index.
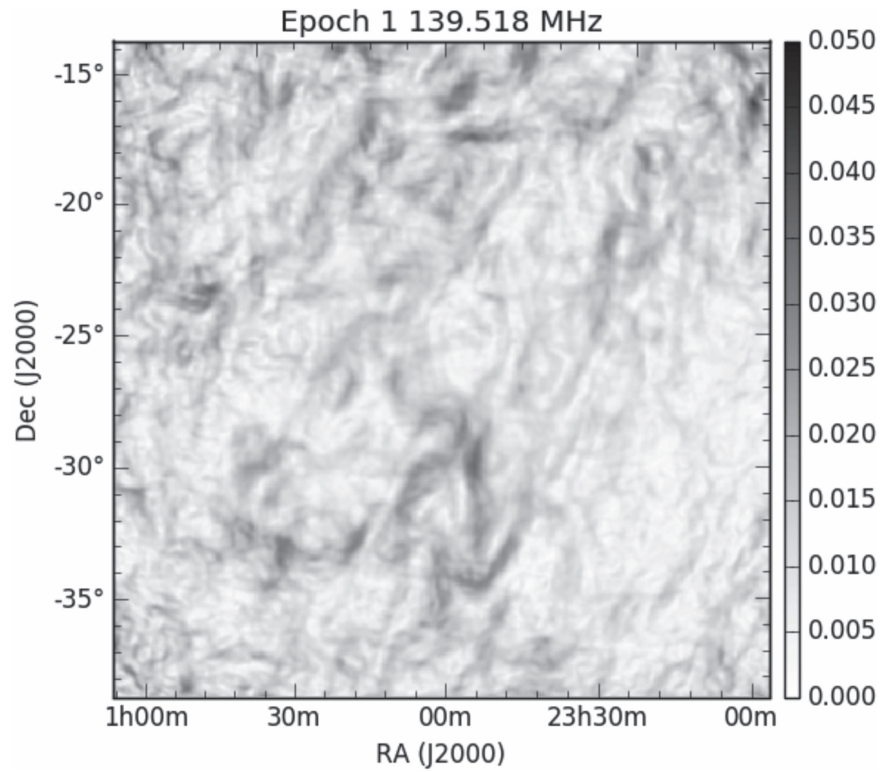
Figure 13. Epoch 1 EoR-0 gradient maps for 24×1.28 MHz channels across the 154 MHz band.
(An animation of this figure is available.)
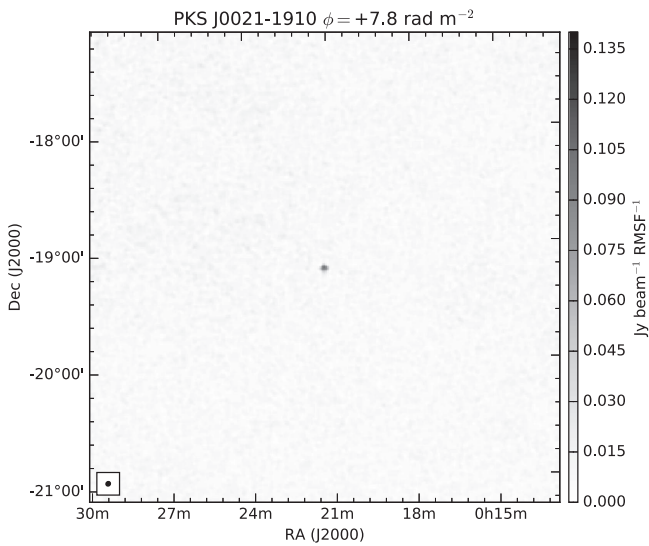
Figure 14. Cut-out showing the polarized source PKS J0021−1910. The synthesized beam is $2'.2 \times 2'.4$ FWHM with a position angle of $-47°$.

uniform synchrotron emissivity, electron density, and magnetic field in a volume of ISM, the path length L at which integrated emission is totally depolarized is defined as (Uyanıker et al. 2003)

$$L \sim \frac{\pi}{(0.81\lambda^2 n_e B_\parallel)}. \quad (6)$$

Here n_e is the electron density (cm^{-3}), λ is the wavelength (m), and $B_\parallel$ is the magnetic field parallel to the line of sight (μG). We assume an electron density of $n_e = 0.015\,\mathrm{cm}^{-3}$,
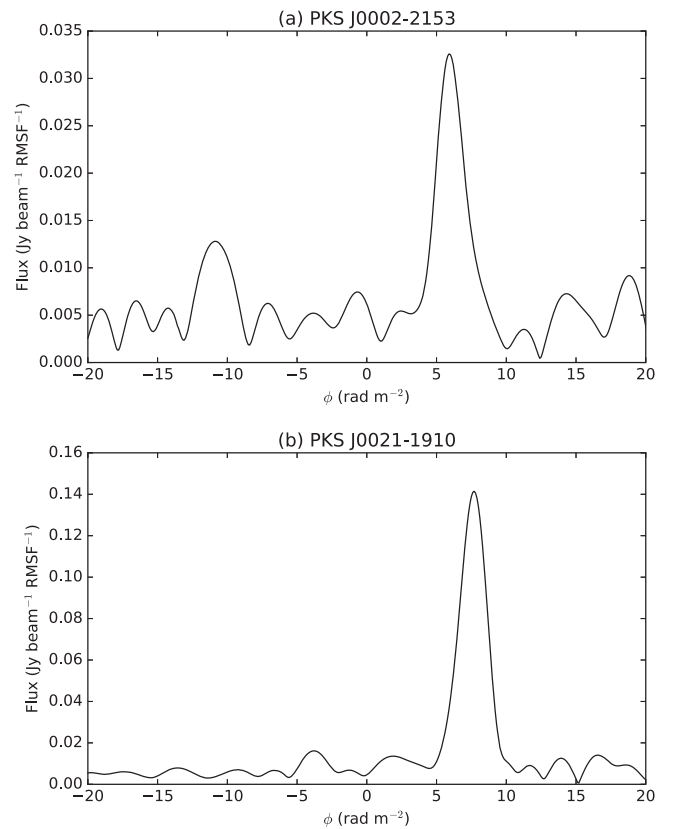
Figure 15. Sources detected with high-resolution imaging. (a) Faraday dispersion function for PKS J0002–2153. RM $= +5.7\,\mathrm{rad\,m}^{-2}$. Noise is 2.5 mJy beam^{-1} RMSF^{-1} rms. (b) Faraday dispersion function for PKS J0021–1910. RM $= +7.8\,\mathrm{rad\,m}^{-2}$. Noise is 3.1 mJy beam^{-1} RMSF^{-1} rms.
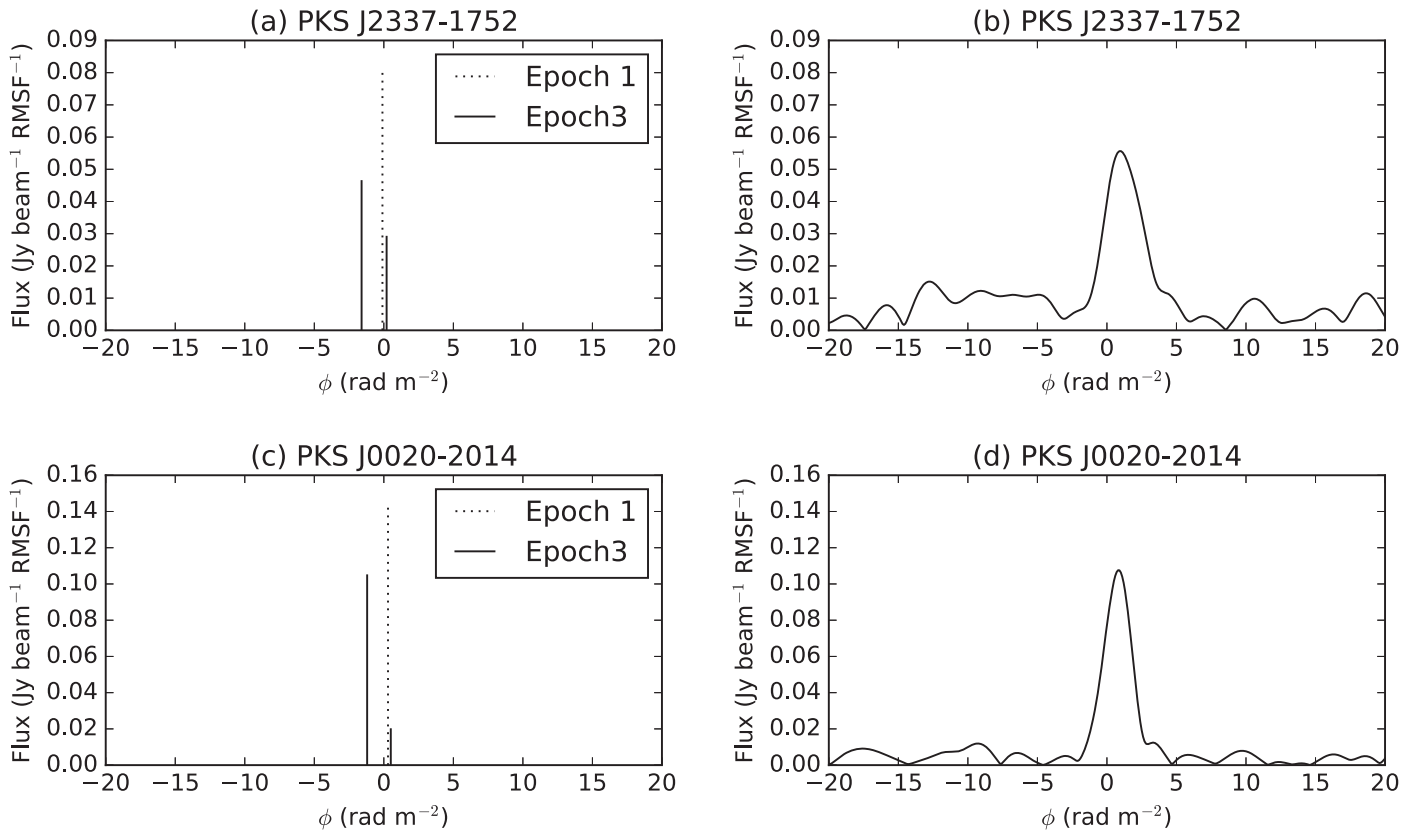
Figure 16. Sources found in a multi-epoch analysis that distinguishes real sources from instrumental effects by searching for peaks shifted in Faraday space as a result of ionospheric Faraday rotation. (a) Peaks detected in RM synthesis in epochs 1 and 3 for PKS J2337–1752 before correcting for the effects of ionospheric Faraday rotation. (b) Faraday dispersion function for PKS J2337–1752 in epoch 3 after correcting for the effects of ionospheric Faraday rotation. RM = +0.8 rad m^{-2}. Noise is 3.9 mJy beam^{-1} RMSF^{-1} rms. (c) Peaks detected in RM synthesis in epochs 1 and 3 for PKS J0020–2014 before correcting for the effects of ionospheric Faraday rotation. (d) Faraday dispersion function for PKS J0020–2014 in epoch 3 after correcting for the effects of ionospheric Faraday rotation. RM = +1.0 rad m^{-2}. Noise is 3.4 mJy beam^{-1} RMSF^{-1} rms.

which is consistent with most estimates of the volume-average electron density in the thick-disk component of the warm ionized medium (Gaensler et al. 2008). We can estimate $B_{\parallel}$ using the local horizontal field of $\sim 2.0\,\mu$G (Beck et al. 1996) projected for the direction of the observation; this gives $B_{\parallel} = 0.6\,\mu$G. At the center of the MWA band, total depolarization occurs at a distance of $L \sim 125$ pc and so most polarized features observed can be assumed to be at $\lesssim 125$ pc. This estimate contains uncertainties with respect to the value of n_e and $B_{\parallel}$ used in the direction of the the EoR field. We also note that at path-lengths beyond the polarization horizon, the radiation is partially repolarized again (Burn 1966; Sokoloff et al. 1998) and so some fraction of emission will exist from beyond the horizon. An even greater uncertainty exists with respect to beam depolarization, which will be significant at MWA wavelengths. However, as the observed polarized structures are larger in extent than the MWA beam and exhibit smooth features in Faraday space (see Figure 6) this effect may not be as great in this instance.

A third estimate of the distance to the emission can be derived from known pulsars within the field. This approach is similar to the first approach, which used the RM contribution of the Galaxy, but relies on the RM toward a nearby pulsar to reduce the uncertainty associated with current models of the Galaxy. Using this approach, the distance L to the polarized emission can be estimated as

$$L = \frac{d_{\text{pulsar}} \times \text{RM}}{\text{RM}_{\text{pulsar}}}. \qquad (7)$$

Here d_{pulsar} is the distance to the pulsar, RM is the measured RM from the polarized emission and $\text{RM}_{\text{pulsar}}$ is the RM of the pulsar.

The diffuse polarized emission in the EoR-0 field has an RM distribution that peaks at $+1.0 \pm 0.3$ rad m^{-2}. A search through the ATNF Pulsar Catalog[31] v1.54 (Manchester et al. 2005) revealed a single known pulsar within the EoR-0 field, PSR J2330–2005 (see Figure 5). The pulsar has a dispersion measure (DM) of 8.456 ± 0.002 pc cm^{-3} (Stovall et al. 2015), an estimated DM-based distance of 490 ± 100 pc (Taylor & Cordes 1993) and an RM of $+16 \pm 3$ rad m^{-2} (Hamilton & Lyne 1987). Based on these parameters, this would place the polarization emission at a distance of 31 ± 12 pc.

In our targeted search of the pulsar field, we detect PSR J2330–2005 in both linear and circular polarization. In linear polarization, we consistently find a weak 19 mJy beam^{-1} peak (14% fractional polarization) and measure an RM of $+9.6 \pm 0.1$ rad m^{-2} in both epochs 1 and 3. The measured RM is lower than that reported in the ATNF Pulsar Catalog.

_____

[31] http://www.atnf.csiro.au/research/pulsar/psrcat

19

Table 3
Details of Polarized Point Sources Detected in the EoR-0 Field

| Source	RM_{MWA} (rad m^{-2})	RM_{lit} (rad m^{-2})	P_{MWA} (mJy beam^{-1})	p_{MWA}	p_{lit}	ν_{obs} (MHz)	DP(1400, 154)
PSR J2330–2005	+9.6 ± 0.1	+16 ± 3[a]	19	14%	16%	648[b]	
		+9.5 ± 0.2[a]					
		+9.5 ± 0.6[c]					
PKS J2337–1752	+0.6 ± 0.1	+12.2 ± 1.3[d]	46	1.3%	3.67 ± 0.07%	1400[d]	0.26
PKS J0002–2153	+5.8 ± 0.1	+6.0 ± 4.9[d]	33	2.1%	6.0 ± 4.9%	1400[d]	0.32
PKS J0020–2014	+1.6 ± 0.1	+1.5 ± 2.7[d]	105	3.5%	12 ± 1.3%	1400[d]	0.37
PKS J0021–1910	+7.9 ± 0.1	+3.6 ± 5.2[d]	140	3.0%	3.6 ± 5.2%	1400[d]	0.91

Notes. RM_{MWA} is the rotation measure determined from MWA observations (corrected for ionospheric faraday rotation). RM_{lit} is the rotation measure in literature. P_{MWA} and p_{MWA} are the polarized flux density and fraction polarization derived from MWA observations, respectively. p_{lit} is the fractional polarization in literature, at an observing frequency of ν_{obs}. DP(1400, 154) is the depolarization ratio from 1.4 GHz to 154 MHz.
[a] Hamilton & Lyne (1987).
[b] McCulloch et al. (1978).
[c] Johnston et al. (2007).
[d] Taylor et al. (2009).
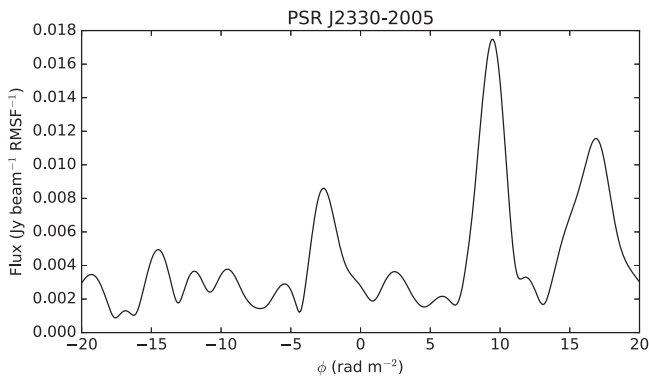
Figure 17. Faraday dispersion function for PSR J2330–2005 from epoch 1 after correcting for the effects of ionospheric Faraday rotation. RM = +9.6 rad m^{-2}. Noise is 1 mJy beam^{-1} RMSF^{-1} rms.

However, Hamilton & Lyne (1987) report an RM of +9.5 ± 0.2 rad m^{-2} from unpublished observations and Johnston et al. (2007) measure an RM of +9.5 ± 0.6 rad m^{-2}, both of which are highly consistent with our measurement. If we take our measured RM instead of the RM from the ATNF Pulsar Catalog, we place the distance to the polarized emission at 51 ± 20 pc. Based on the measured RM to the pulsar, we estimate the average electron density on the line of sight of this pulsar to be 0.0183 ± 0.002 cm^{-2} and the magnetic field $B_{\parallel} = 1.31 \pm 0.01\ \mu$G; these are consistent with those expected in the solar neighborhood.

We recognize that the estimate of the distance toward the polarized emission of ~110–220 pc, based on the estimated contribution of Galactic RM toward extragalactic sources, and the $L \lesssim 125$ pc distance based on depth depolarization contain significant uncertainties. The estimate based on a relatively nearby pulsar within the observed field, however, is only limited by uncertainties in the measured distance of the pulsar and any inhomogeneities that may exist in the magnetic field and electron density toward the pulsar. As such, we adopt 51 ± 20 pc as our estimate of the distance toward the observed polarized emission.

### 4.4. Polarized Point-source Population

Based on Taylor et al. (2009) observations at 1.4 GHz, there are 399 known polarized sources within the 400 sq. degree region of the EoR-0 field. The 154 MHz flux density of these sources, in total intensity, cannot be accurately determined from the high-resolution MWA maps shown in Figure 2 because the field suffers greatly from sidelobe confusion. Instead, the spectral slope of each source can be determined by comparing the 1.4 GHz Taylor et al. (2009) observations with 158 MHz GLEAM observations of the field (Hurley-Walker et al. 2016, in preparation). Based on the measured spectral slopes and assuming no depolarization, one would expect ~191 of the Taylor et al. (2009) 1.4 GHz sources to be detected in polarization at 154 MHz. In all, only four of these sources were detected at 154 MHz with the MWA.

It is useful to consider the depolarization ratio for the sources within the MWA field. We determine the depolarization ratio (DP) between 1.4 GHz and 154 MHz using (Beck 2007):

$$DP(1400, 154) = (P_{154}/P_{1400})(1400/154)^{\alpha} \qquad (8)$$

where α is the measured spectral index of the source. DP(1400, 154) = 1 when there is no change in fractional linear polarization from 1.4 GHz to 154 MHz, i.e., no depolarization. DP(1400, 154) = 0.5 when the fractional linear polarization at 154 MHz is half that at 1.4 GHz. In order to depolarize all remaining 187 Taylor et al. (2009) sources at 154 MHz to below the sensitivity limits of the MWA observations, a DP(1400, 154) upper limit of <0.08 would be required.

Mulcahy et al. (2014) searched for polarized sources in a deep 8 hr 151 MHz LOFAR observation around M51 with significantly higher resolution (20″) and sensitivity (100 μJy beam^{-1}), albeit over a much smaller field-of-view (17 square degrees). In all, a total of six polarized sources were detected. Three of the sources have Taylor et al. (2009) counterparts and have a measured DP(1400, 151) of 0.196, 0.038, and 0.029. These depolarization ratios would be consistent with those required to depolarize all known 1.4 GHz polarized sources in our MWA field-of-view even without taking into consideration the additional beam
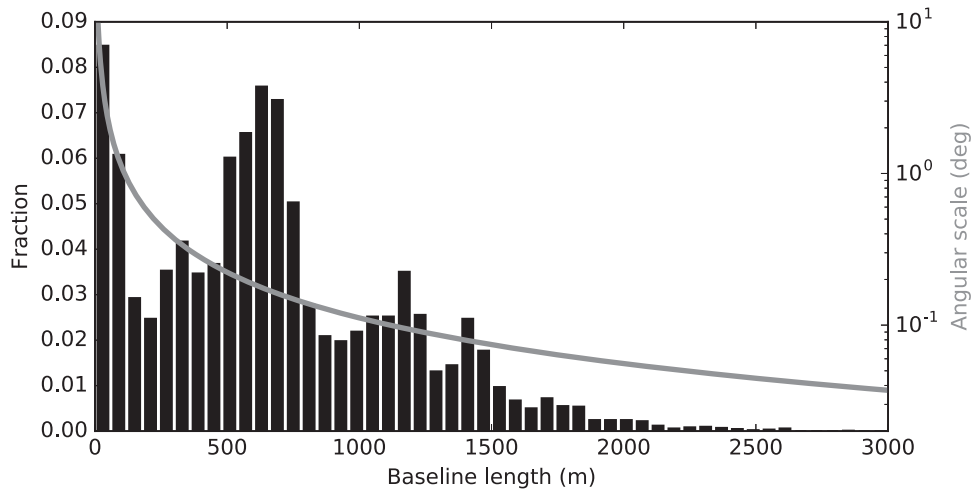
Figure 18. Snapshot imaging baseline distribution for MWA 128T when observing at zenith ($\delta = -26°.7$). The gray curve plots the angular scale probed as a function of baseline length.

depolarization that would be expected with the larger MWA beam.

While it is beyond the scope of this paper to analyze further, it is interesting to note that the four extragalactic sources detected with the MWA are not significantly more depolarized at 154 MHz compared to 1.4 GHz, i.e., DP(1400, 154) ranges between 0.26 and 0.91 (see Table 3). As such, they are characteristically different to the sources detected by Mulcahy et al. (2014) with LOFAR and the MWA field sources that have clearly depolarized below our detection threshold. This could hint at a very small population of sources (one per 100 sq. deg) that do not show significant changes in depolarization with wavelength. The population is small enough that LOFAR may not yet have observed such sources with the limited number of fields observed in full polarization with its smaller field of view. We do note, however, that two of the least depolarized sources detected with the MWA are associated with unresolved polarized hot spots of relatively large radio galaxies (0.27 and 1.22 Mpc in extent). If these hot spots lie outside the local environment of the host galaxy, they may not suffer as greatly from the effects of depolarization as ones that are embedded within a magnetized plasma.

4.5. Turbulence in the ISM

The structures seen in polarization gradient maps are generally caused by differential Faraday rotation (Shukurov & Berkhuijsen 2003; Fletcher & Shukurov 2007), a foreground Faraday screen (Haverkorn & Heitsch 2004; Fletcher & Shukurov 2007; Gaensler et al. 2011), or intrinsic emission (Sokoloff et al. 1998; Sun et al. 2014).

Differential Faraday rotation causes depolarization contours that may manifest themselves as polarization gradients. They arise where synchrotron emission and Faraday rotation occur in the same region. For a given wavelength (λ), depolarization occurs at position x in the plane of the sky under the condition where $2|RM(x)|\lambda^2 = \pi n$ (Shukurov & Berkhuijsen 2003) and $n = 1,\ 2,\ 3,\ldots$ The resulting depolarization contours are infinitely thin, i.e., unresolved by the beam, and will shift as a function of frequency. As such, the contours in this interpretation are not directly related to any real structures in the ISM—hence the alternate name of "Faraday ghosts."

A second interpretation of depolarization canals is that they are caused by gradients in a foreground Faraday screen (Fletcher & Shukurov 2007). In this interpretation, features in the radio polarization gradient map are physically associated with specific structures in the ISM. These structures are caused by a sudden increases or decreases of the electron density or magnetic field. As such, these features remain spatially fixed but appear and disappear as a function of frequency as different depths are probed. Features exhibiting such behavior have been observed at centimeter wavelengths, see Gaensler et al. (2011), but the evolution of these features has not yet been explored over large fractional bandwidths.

A third interpretation is that the features are intrinsically polarized and caused by random anisotropic magnetic fields (Shukurov & Berkhuijsen 2003). This results in smooth synchrotron emission in total intensity, which is not observable since it is spatially filtered by the instrument, but with intrinsically polarized structures on smaller scales that are observable. In general, the structures will not shift or evolve as a function of frequency; however, more distant features will only be seen at shorter wavelengths as a result of the polarization horizon (see Section 4.3). As such, there will be an increase in the number of observed features as a function of increasing frequency.

The three different interpretations can be easily distinguished with a multi-frequency analysis of the gradient maps. We have shown that significant features are observed in the EoR gradient maps when full-band 154 MHz data are utilized (Figure 11). These features are of the order of $1°$ in extent and are consistent with the beam size, i.e., unresolved. Assuming a distance of 51 ± 20 pc, they have a spatial extent of 0.9 ± 0.3 pc, which is consistent with the $\sim$0.5 pc spatial extent observed in similar unresolved features in the Galactic plane at 1.4 GHz (Gaensler et al. 2011). These gradient map features are also present in multi-band GLEAM snapshot data (Figure 12), but the maps are limited by poor sensitivity and instrumental leakage, which affect the higher frequency end of the band.

The deep epoch 1 observations, however, provide sufficient sensitivity on a per-160 kHz channel basis to examine the frequency-dependent behavior of the gradient function, see Figure 13. If we consider the polarization horizon, as described in Equation (6), the gradient function cube explores a square

frustum centered on the EoR-0 field. In this instance, the back of the frustum (upper end of the observing band) probes more deeply (polarization horizon of 150 pc) and the front of the frustum (lower end of the observing band) probes nearby features (polarization horizon of 100 pc).

When the gradient function cube is explored, the gradient features vary smoothly as a function of frequency but show no significant spatial movement. The lack of spatial translation of the features rules out the differential Faraday rotation interpretation. Furthermore, most features that peak at the lower end of the band tend to persist toward the higher end of the band, with an accumulation of features with increasing frequency. This observation tends to support an intrinsic polarization interpretation but does not completely rule out a foreground Faraday screen (which generally results in features that do not vary as a function of wavelength).

A limitation of the polarization gradient method is that it is only sensitive to structures that have a scale-size similar to that of the synthesized beam of the instrument (Robitaille & Scaife 2015). Gradient features larger than the beam size are resolved spatially in the plane of the sky. The same is not true for features that extend spatially in a direction perpendicular to the plane of the sky since the gradient function is only performed over the two spatial dimensions and not in the frequency direction (which, as described in the previous paragraph, can act as a proxy for depth). This may result in features appearing larger in depth than in spatial extent and confuse the distinction between features caused by interpretations 2 and 3 above.

To distinguish between interpretations 2 and 3, we can determine whether the observed RM gradient in the field is sufficiently large enough to result in the polarization gradients we observe. If an RM gradient results in a polarization gradient then this is evidence of a foreground Faraday screen (interpretation 2). However, if a polarization gradient appears where there is no clear RM gradient, then this is evidence of intrinsic polarization (interpretation 3). To test this, we consider a uniform linearly polarized background:

$$\boldsymbol{P} = P_0 e^{2i(\psi + \phi\lambda^2)} \qquad (9)$$

where ψ is the intrinsic polarization angle, ϕ is the Faraday depth, and P_0 is magnitude of the polarized intensity. From this equation, assuming P_0 is constant, the relationship between the polarization gradient ($|\boldsymbol{\nabla P}|$) and RM gradient ($|\nabla \phi|$) for Faraday-thin polarized emission can be derived as (Burkhart et al. 2012)

$$|\boldsymbol{\nabla P}| = 2\lambda^2 P_0 |\nabla \phi|. \qquad (10)$$

The intrinsic polarized intensity, P_0, cannot be obtained from our MWA observations directly because of depolarization. Instead, we can estimate it based on the intensity of synchrotron emission out to our adopted distance of the polarized emission. Nord et al. (2006) estimate a local emissivity of $\epsilon_{74} = 0.36 \pm 0.17 \, \mathrm{K \, pc}^{-1}$ at 74 MHz. Taking a distance of 51 ± 20 pc, the estimated total intensity is $500 \pm 300 \, \mathrm{mJy \, beam}^{-1}$ assuming a temperature spectral index of $\beta = -2.55$ (see Section 4.2). If we assume approximately 30% intrinsic polarization (Sun et al. 2008) this equates to $P_0 = 150 \pm 90 \, \mathrm{mJy \, beam}^{-1}$ at 154 MHz. Similarly, Peterson & Webber (2002) estimate $\epsilon_{10} = 3.0 \pm 0.7 \times 10^{-40} \, \mathrm{W \, m}^{-3} \, \mathrm{Hz}^{-1} \, \mathrm{sr}^{-1}$ at 10 MHz. Using the same assumptions as above, this results in $P_0 = 530 \pm$

$230 \, \mathrm{mJy \, beam}^{-1}$. At 154 MHz, these estimates suggest that a $0.01 \, \mathrm{rad \, m}^{-2} \, \mathrm{beam}^{-0.5}$ RM gradient would result in a $0.011 \pm 0.007 \, \mathrm{Jy \, beam}^{-1.5}$ gradient in polarization for the Nord et al. (2006) estimate and $0.040 \pm 0.017 \, \mathrm{Jy \, beam}^{-1.5}$ gradient for the Peterson & Webber (2002) estimate.

We can compare this with our observed gradients. Figure 19 shows the RM, RM gradient, and polarization gradient in a region of the EoR-0 field, where significant gradients are observed in polarization. There is one clear RM gradient feature, the S-shaped feature on the left of the RM gradient map running from top to bottom, that is associated with one of the filaments observed in the polarization gradient map. The feature peaks at $\sim 0.02 \, \mathrm{rad \, m}^{-2} \, \mathrm{beam}^{-0.5}$ in the RM gradient map and at $\sim 0.024 \, \mathrm{Jy \, beam}^{-1.5}$ in the polarization map. This particular feature seems consistent with a polarization gradient resulting from a Faraday screen in which $P_0 = 160 \, \mathrm{mJy \, beam}^{-1}$, a value that is within the Nord et al. (2006) and Peterson & Webber (2002) estimates. The structure is reminiscent of the Burkhart et al. (2012) "Case 2" scenario associated with supersonic- and subsonic-type turbulence. In this scenario, there is a jump in RM spatially as a result of strong turbulent fluctuations in the magnetic field or electron density along the line of sight, weak shocks, or edges of a foreground cloud.

The brightest polarization gradient feature, just west of the S-shaped feature in Figure 19, has no obvious counterpart in the RM gradient map. It is likely that this, and similar features throughout the wider field, are polarization gradients resulting from intrinsically polarized structures and are not caused by foreground Faraday screens. The presence of polarization gradients with RM gradient counterparts and also those without counterparts hint that the observed polarized structure results from a combination of both instrinsically polarized structures and a foreground Faraday screen.

4.6. Structure Function

In Section 4.5, we investigated possible causes for the structures seen in the polarization gradient maps and concluded that they could result from a combination of both instrinsically polarized structures and a foreground Faraday screen. An alternate method of distinguishing between these two causes is through a structure function analysis (Sun et al. 2014). The structure function of complex polarization ($P = Q + iU$) and that of polarized intensity ($p = |P|$) are defined respectively as

$$\mathrm{SF}_P(\delta\theta) \equiv \langle |P(\theta) - P(\theta + \delta\theta)|^2 \rangle \qquad (11)$$

$$\mathrm{SF}_p(\delta\theta) \equiv \langle [p(\theta) - p(\theta + \delta\theta)]^2 \rangle \qquad (12)$$

Here $\delta\theta$ is the angular separation between two lines of sight. A comparison of the two structure functions can indicate whether the observed polarized structures are intrinsic or caused by Faraday screens (Sun et al. 2014). For intrinsic polarization, there will be no correlation between polarized intensity and polarization angle, so the slope of SF_p will be similar to that of SF_P. Alternatively, if the polarized structures are caused by Faraday screens with beam depolarization, then the slope of SF_P will be flatter than SF_p since much of the intrinsic structure will be smeared out by Faraday screens.

The resulting structure functions for SF_p and SF_P are shown in Figure 20 for epoch 1 observations of the EoR-0 field. At angular separations less than about $90'$, the slope of the structure function effectively represents the smoothing effect of the MWA PSF ($54'$). At very large angular separations, the
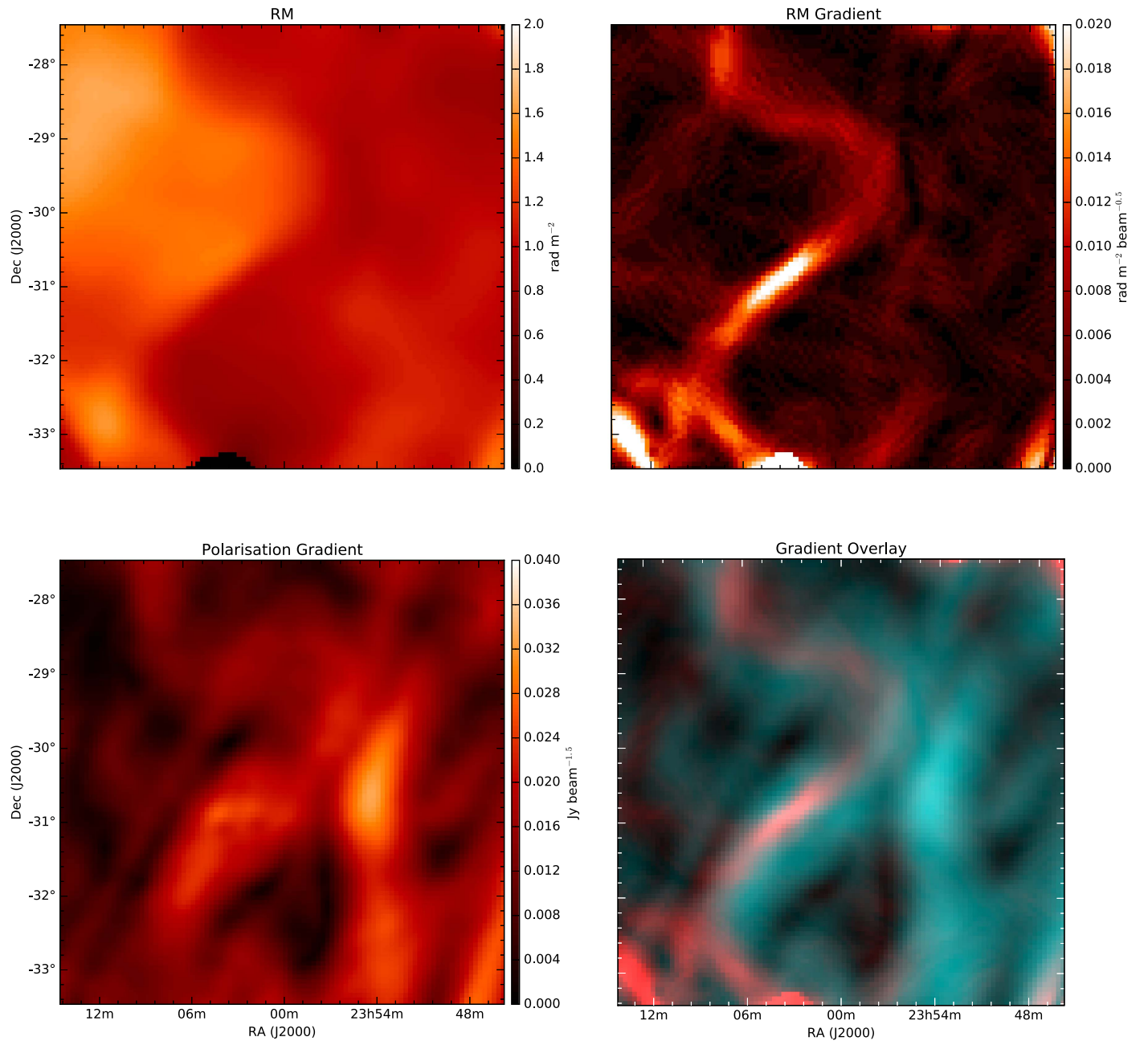
Figure 19. Zoomed in view of a region containing both significant polarized flux and smooth RM variations. (Top left) Map showing RM (rad m^{-2}) at peak polarized intensity for each pixel in the Faraday depth cube. The map is the same as that highlighted by the dashed square in Figure 6 but with a color scale that highlights finer variations in RM. (Top right) The rotation measure gradient map (rad m^{-2} beam$^{-0.5}$) − |∇ϕ|. This is the spatial gradient of the RM map (shown in the top left). (Bottom left) The polarization gradient map (Jy beam$^{-1.5}$) − |∇**P**|. The map is the same as that highlighted by the dashed square in Figure 12 for the time-averaged and band-averaged epoch 1 data but with a different color scale. (Bottom right) Overlap map of RM gradient (red) and polarization gradient (cyan).

structure function is less constrained because of limited sensitivity of the MWA to structures ≳10° and the available field of view (25° × 25°). For this analysis, we focus on the region between $120' < \delta\theta < 270'$ to avoid data affected by instrumental constraints. We note that there is observed curvature in the structure function for SF$_P$ in the fitting region, possibly associated with a contaminating sidelobe structure. While this results in a poorer fit for SF$_P$ compared to that of SF$_p$, the slope of SF$_P$ is consistent to, or at most steeper, than that of SF$_p$. If the slope of SF$_P$ were flatter than that of SF$_p$ this would be suggestive of polarization caused by Faraday screens (Sun et al. 2014). However, the similarity in slope of SF$_p$ and

SF$_P$, within 3σ fitting errors, suggests that the structures are dominated by intrinsic polarization.

In observations of the Galactic plane at 4.8 GHz, Sun et al. (2014) also find evidence of intrinsic polarization whereas at 2.3 GHz a structure function analysis suggests the presence of a Faraday screen. The reasoning for the different behavior is that higher frequency observations (4.8 GHz) probe more deeply because they are less affected by the presence of a Faraday screen. One would expect that MWA observations would be particularly sensitive to the effects of a Faraday screen because they are observed at long wavelengths. However, the structure function analysis suggests that the observed diffuse
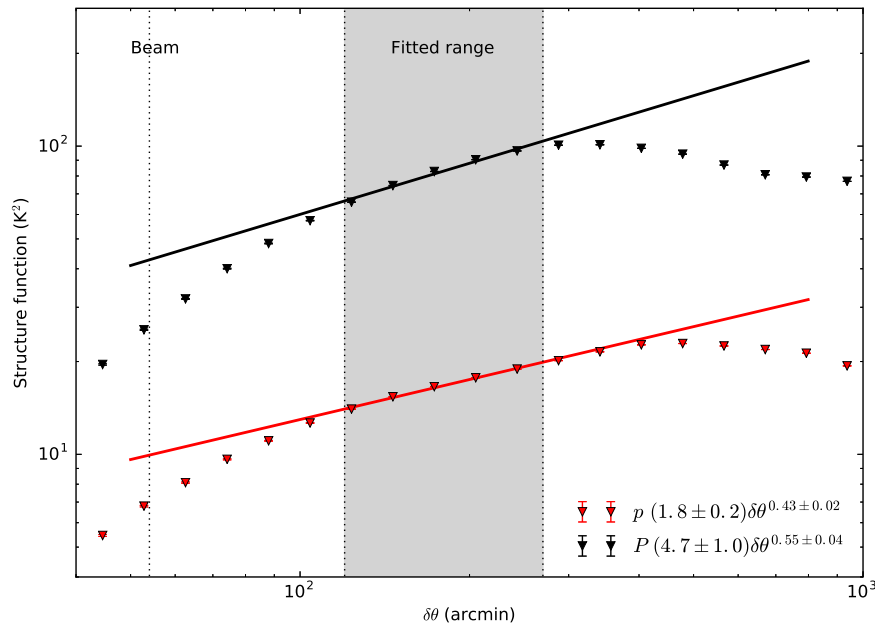
Figure 20. Structure function for epoch 1 data in the EoR-0 field using ionosphere-corrected continuum images. The fit to the curve in the region marked in gray ($120' < \delta\theta < 270'$) is shown for both p and P. The beam is marked by a dotted line at $54'$. The noise floor is not shown here but it is approximately four orders of magnitude below each of the fitted curves.

polarization is intrinsic in nature and must therefore be associated with structures that are very local.

The structure function analysis performed here suggests that intrinsic polarization is dominating in this field. This is consistent with the multi-frequency polarization gradient analysis performed in Section 4.5, which found evidence of both intrinsic and Faraday screen causes for the observed polarization gradients. Currently, the structure function analysis is limited by the effective range of angular separations that could be used. Deconvolution and imaging of even larger fields would aid in widening this range and improving the structure function analysis; however, this will be left for future work.

4.7. Faraday Depth Structure

As described in Section 3.3, the 154 MHz MWA observations provide a narrow RMSF of $\delta\phi = 2.3$ rad m^{-2}. Combined with the maximum-scale size sensitivity of 1.0 rad m^{-2} the MWA observations are only able to detect simple components even in the presence of Faraday complex structure. The presence of a Faraday-thick structure would be entirely resolved by the MWA RMSF, resulting in a two-peak FDF (see Figure 3, Li et al. 2011). A Faraday-thin structure, however, would result in a simple FDF with a single component; see Appendix B of Brentjens & de Bruyn (2005).

A mix of structures has been observed in Faraday spectra observed in the Galactic anti-center with the WSRT at 324–387 MHz with $\sim 3'$ resolution (Schnitzeler et al. 2007, 2009). The vast majority of lines of sight observed in a $9° \times 9°$ field have Faraday spectra that are reasonably well fit by a simple model dominated by a single bright peak. Only a small fraction of lines of sight exhibit Faraday complexity.

Looking at the Faraday spectra from the 154 MHz MWA EoR-0 observations, the vast majority of Faraday structure is simple and dominated by peaks at low RM; see Figures 7 and 8. This indicates that the extent of the polarized emission in Faraday depth is less than the MWA RMSF. The Faraday

spectra are similar to those observed in diffuse polarization at similar wavelengths with LOFAR in the ELAIS-N1 (Jelić et al. 2014) and 3C196 fields (Jelić et al. 2015) with a narrower RMSF (0.9 rad m^{-2}). It is unlikely that these are unresolved Faraday-thick structures because of the excellent resolution available in Faraday space with the MWA and LOFAR. Without introducing a more involved scenario, in which a secondary peak in Faraday space is weakened to a level below our detection threshold, a simple explanation of the peak is that the polarized emission is Faraday-thin, meaning the polarized structure is intrinsic. This would be consistent with findings of the polarization gradient function analysis and the structure function analysis discussed in Sections 4.5 and 4.6.

5. CONCLUSIONS

We have presented a 625 square degree survey of diffuse linear polarization at 154 MHz carried out with the MWA. The survey, centered on the MWA EoR-0 field (0^h, $-27°$), achieved a sensitivity of 5.9 mJy beam^{-1} at $\sim 54'$ resolution. The compact baselines of the MWA have been shown to be particularly sensitive to diffuse structures spanning $1°$–$10°$, something that has traditionally only been within reach of single-dish instruments.

Our MWA observations reveal smooth large-scale diffuse structures that are $\sim 1°$–$8°$ in extent in linear polarization and clearly detected even in 2 minute snapshots. The brightness temperature of these structures is, on average, 4 K in polarized intensity, peaking at 11 K. We estimate a distance of 51 ± 20 pc to the polarized emission based on RM measurements of the in-field pulsar PSR J2330–2005.

Rotation measure synthesis reveals that the structures have Faraday depths ranging from -2 to 10 rad m^{-2}. A large fraction of these peak at $+1.0$ rad m^{-2} but smaller structures are also observed to peak at $+3.0$, $+7.1$, and $\sim +9$ rad m^{-2}. The observed RM structure is smooth, particularly around the

region where polarized intensity peaks, with a peak RM gradient of ~ 0.02 rad m^{-2} beam$^{-0.5}$.

The sensitivity available in our deep observations allowed a frequency-dependent analysis of the polarized structure to be performed for the first time at long wavelengths. The results of the analysis suggested that the polarized structures are dominated by intrinsic emission but may also have a component that is due to a foreground Faraday screen. A structure function analysis of our linearly polarized images and an analysis of Faraday structure also suggest that intrinsic polarized emission tends to dominate.

A 400 square degree subset of the field was re-imaged at full resolution ($\sim 2'4$) and 2.3 mJy beam^{-1} sensitivity to search for polarized point sources. We detect four extragalactic linearly polarized point sources within the EoR-0 field and have confirmed these by observing the shift in their RM over two epochs as a result of observably different ionospheric conditions in those epochs. Based on known polarized field sources at 1.4 GHz and non-detections at 154 MHz, we estimate an upper limit on the depolarization ratio of 0.08 from 1.4 GHz to 154 MHz. Such levels of depolarization are not surprising at long wavelengths; however, we note that the four detected sources did not exhibit significantly increased levels of depolarization compared to 1.4 GHz. This may hint toward a small population of sources (one per 100 sq. deg) with this behavior. We also note that these may be associated with relatively large radio galaxies where unresolved polarized hot spots lie outside of the local environment and are less likely to suffer the effects of depolarization.

With its high sensitivity to large-scale structure, the MWA has proven itself to be a formidable instrument for the study of diffuse polarization in the local ISM. In combination with RM synthesis, it also provides a unique ability to measure the effect of ionospheric Faraday rotation on the diffuse polarized background both spatially ($\sim 1°$ resolution) and temporally (~ 2 minute resolution). This not only allows ionospheric effects to be calibrated without the need for ionospheric models but also provides an opportunity to observe local solar events by measuring their effect on the background RM.

The survey presented in this paper utilized only a very small fraction of the data currently available in the EoR and GLEAM projects. There is great potential to extend the survey to look more deeply within the EoR fields, to look over an increased field of view with the GLEAM data, and also to explore the full 80–230 MHz range of frequencies available in the GLEAM data. Additional epochs of GLEAM data will aid in improving sensitivity and mitigating the sidelobe confusion that affects some snapshots. An implementation of an improved beam model will drastically reduce the apparent leakage observed in the highest frequency bands and so increase the range of reliable data available for subsequent frequency-dependent analysis. Furthermore, deconvolution of the diffuse structure and a multi-scale analysis of the gradient of linear polarization, e.g., Robitaille & Scaife (2015), would allow the observations to probe more deeply.

While the sensitivity of the observations presented in this paper prevented such an analysis, a measurement of instrumental leakage from linear polarization into total intensity would provide valuable information to the EoR community. Understanding leakage of this form is of particular importance for EoR science because it can act as a possible contamination source for EoR measurements (Jelić et al. 2008; Geil

et al. 2011; Moore et al. 2013; Asad et al. 2015). This has been left for future work and will be performed once the new MWA beam model has been implemented. An improved analysis will also be possible with an extension to the MWA that is currently underway. The extension provides additional compact configurations and redundant baselines that will aid in calibration.

REFERENCES

Arora, B. S., Morgan, J., Ord, S. M., et al. 2015, PASA, 32, e029
Asad, K. M. B., Koopmans, L. V. E., Jelić, V., et al. 2015, MNRAS, 451, 3709
Baars, J. W. M., Genzel, R., Pauliny-Toth, I. I. K., & Witzel, A. 1977, A&A, 61, 99
Beck, R. 2007, A&A, 470, 539
Beck, R., Brandenburg, A., Moss, D., et al. 1996, ARA&A, 34, 155
Berdyugin, A., Piirola, V., & Teerikorpi, P. 2004, A&A, 424, 873
Berdyugin, A., Piirola, V., & Teerikorpi, P. 2014, A&A, 561, A24
Berdyugin, A., & Teerikorpi, P. 2001, A&A, 368, 635
Berkhuijsen, E. M., Mitra, D., & Mueller, P. 2006, AN, 327, 82
Bernardi, G., de Bruyn, A. G., Brentjens, M. A., et al. 2009, A&A, 500, 965
Bernardi, G., de Bruyn, A. G., Harker, G., et al. 2010, A&A, 522, A67
Bernardi, G., Greenhill, L. J., Mitchell, D. A., et al. 2013, ApJ, 771, 105
Bowman, J. D., Cairns, I., Kaplan, D. L., et al. 2013, PASA, 30, 31
Brentjens, M. A., & de Bruyn, A. G. 2005, A&A, 441, 1217
Burkhart, B., Lazarian, A., & Gaensler, B. M. 2012, ApJ, 749, 145
Burn, B. J. 1966, MNRAS, 133, 67
Calabretta, M. R., Staveley-Smith, L., & Barnes, D. G. 2014, PASA, 31, e007
Carretti, E. 2010, in ASP Conf. Ser. 438, The Dynamic Interstellar Medium: A Celebration of the Canadian Galactic Plane Survey, ed. R. Kothes, T. L. Landecker, & A. G. Willis (San Francisco, CA: ASP), 276
Ellingson, S. W., Clarke, T. E., Cohen, A., et al. 2009, IEEEP, 97, 1421
Fletcher, A., & Shukurov, A. 2007, EAS Publications Series, 23, 109
Franzen, T. M. O., Jackson, C. A., Callingham, J. R., et al. 2015, The many facets of extragalactic radio surveys: towards new scientific challenges (EXTRA-RADSUR2015) Galaxy Evolution - II (Trieste: SISSA), 53
Gaensler, B. M., Dickey, J. M., McClure-Griffiths, N. M., et al. 2001, ApJ, 549, 959
Gaensler, B. M., Haverkorn, M., Burkhart, B., et al. 2011, Natur, 478, 214
Gaensler, B. M., Madsen, G. J., Chatterjee, S., & Mao, S. A. 2008, PASA, 25, 184
Geil, P. M., Gaensler, B. M., & Wyithe, J. S. B. 2011, MNRAS, 418, 516
Gray, A. D., Landecker, T. L., Dewdney, P. E., & Taylor, A. R. 1998, Natur, 393, 660
Guzmán, A. E., May, J., Alvarez, H., & Maeda, K. 2011, A&A, 525, A138
Hamilton, P. A., & Lyne, A. G. 1987, MNRAS, 224, 1073
Han, J. L., Reich, W., Sun, X. H., et al. 2013, IJMPS, 23, 82
Haslam, C. G. T., Salter, C. J., Stoffel, H., & Wilson, W. E. 1982, A&AS, 47, 1
Haverkorn, M., Akahori, T., Carretti, E., et al. 2015, in Advancing Astrophysics with the Square Kilometre Array, Magnetism (Trieste: SISSA), 96
Haverkorn, M., & Heitsch, F. 2004, A&A, 421, 1011

Haverkorn, M., Katgert, P., & de Bruyn, A. G. 2000, A&A, 356, L13
Haverkorn, M., Katgert, P., & de Bruyn, A. G. 2003a, A&A, 403, 1031
Haverkorn, M., Katgert, P., & de Bruyn, A. G. 2003b, A&A, 403, 1045
Haverkorn, M., Katgert, P., & de Bruyn, A. G. 2003c, A&A, 404, 233
Heald, G. 2009, in IAU Symp. 259, Cosmic Magnetic Fields: From Planets, to Stars and Galaxies (Cambridge: Cambridge Univ. Press), 591
Hurley-Walker, N., Callingham, J. R., Hancock, P. J., et al. 2016, MNRAS, in press, doi:10.1093/mnras/stw2337
Hurley-Walker, N., Morgan, J., Wayth, R. B., et al. 2014, PASA, 31, e045
Iacobelli, M., Burkhart, B., Haverkorn, M., et al. 2014, A&A, 566, A5
Iacobelli, M., Haverkorn, M., & Katgert, P. 2013, A&A, 549, A56
Ishwara-Chandra, C. H., & Saikia, D. J. 1999, MNRAS, 309, 100
Jacobs, D. C., Hazelton, B. J., Trott, C. M., et al. 2016, ApJ, 825, 114
Jelić, V., de Bruyn, A. G., Mevius, M., et al. 2014, A&A, 568, 101
Jelić, V., de Bruyn, A. G., Pandey, V. N., et al. 2015, A&A, 583, 137
Jelić, V., Zaroubi, S., Labropoulos, P., et al. 2008, MNRAS, 389, 1319
Johnston, S., Kramer, M., Karastergiou, A., et al. 2007, MNRAS, 381, 1625
Kaplan, D. L., Tingay, S. J., Manoharan, P. K., et al. 2015, ApJL, 809, L12
Lallement, R., Welsh, B. Y., Vergely, J. L., et al. 2003, A&A, 411, 447
Landecker, T. L., Uyanıker, B., & Kothes, R. 2002, in AIP Conf. Ser. 609, Astrophysical Polarized Backgrounds, ed. S. Cecchini et al. (Melville, NY: AIP), 9
Li, F., Brown, S., Cornwell, T. J., & de Hoog, F. 2011, A&A, 531, A126
Loi, S. T., Murphy, T., Bell, M. E., et al. 2015a, MNRAS, 453, 2731
Loi, S. T., Murphy, T., Cairns, I. H., et al. 2015b, GeoRL, 42, 3707
Loi, S. T., Trott, C. M., Murphy, T., et al. 2015c, RaSc, 50, 574
Manchester, R. N., Hobbs, G. B., Teoh, A., & Hobbs, M. 2005, AJ, 129, 1993
Mao, S. A., Gaensler, B. M., Haverkorn, M., et al. 2010, ApJ, 717, 1170
Mathewson, D. S., & Milne, M. F. 1965, AuJPh, 18, 635
McCulloch, P. M., Hamilton, P. A., Manchester, R. N., & Ables, J. G. 1978, MNRAS, 183, 645
McKee, C. F., & Ostriker, E. C. 2007, ARA&A, 45, 565
Mitchell, D. A., Greenhill, L. J., Wayth, R. B., et al. 2008, ISTSP, 2, 707
Moore, D., Aguirre, J. E., Parsons, A., et al. 2016, ApJ, in press (arXiv:1502.05072)
Moore, D. F., Aguirre, J. E., Parsons, A. R., et al. 2013, ApJ, 769, 154
Mulcahy, D. D., Horneffer, A., Beck, R., et al. 2014, A&A, 568, A74
Nord, M. E., Henning, P. A., Rand, R. J., et al. 2006, AJ, 132, 242
Oberoi, D., & Kasper, J. C. 2004, P&SS, 52, 1415
Offringa, A. R., McKinley, B., Hurley-Walker, N., et al. 2014, MNRAS, 444, 606
Offringa, A. R., Trott, C. M., Hurley-Walker, N., et al. 2016, MNRAS, 458, 1057
Offringa, A. R., van de Gronde, J. J., & Roerdink, J. B. T. M. 2012, A&A, 539, A95
Offringa, A. R., Wayth, R. B., Hurley-Walker, N., et al. 2015, PASA, 32, e008
Oppermann, N., Junklewitz, H., Greiner, M., et al. 2015, A&A, 575, A118
Ord, S. M., Crosse, B., Emrich, D., et al. 2015, PASA, 32, e006
Ord, S. M., Mitchell, D. A., Wayth, R. B., et al. 2010, PASP, 122, 1353
Paul, S., Sethi, S. K., Subrahmanyan, R., et al. 2014, ApJ, 793, 28
Peterson, J. D., & Webber, W. R. 2002, ApJ, 575, 217
Prasad, P., Wijnholds, S. J., Huizinga, F., & Wijers, R. A. M. J. 2014, A&A, 568, A48
Puspitarini, L., Lallement, R., Vergely, J.-L., & Snowden, S. L. 2014, A&A, 566, A13
Reid, R. I., Kronberg, P. P., & Perley, R. A. 1999, ApJS, 124, 285
Remazeilles, M., Dickinson, C., Banday, A. J., et al. 2015, MNRAS, 451, 4311
Robitaille, J.-F., & Scaife, A. M. M. 2015, MNRAS, 451, 372
Sault, R. J., Hamaker, J. P., & Bregman, J. D. 1996, A&AS, 117, 149
Sault, R. J., Teuben, P. J., & Wright, M. C. H. 1995, in ASP Conf. Ser. 77, Astronomical Data Analysis Software and Systems IV, ed. R. A. Shaw, H. E. Payne, & J. J. E. Hayes (San Francisco, CA: ASP), 433
Schnitzeler, D. H. F. M., Katgert, P., & de Bruyn, A. G. 2007, A&A, 471, L21
Schnitzeler, D. H. F. M., Katgert, P., & de Bruyn, A. G. 2009, A&A, 494, 611
Shukurov, A., & Berkhuijsen, E. M. 2003, MNRAS, 342, 496
Slee, O. B. 1977, AuJPA, 43, 1
Slee, O. B. 1995, AuJPh, 48, 143
Sokoloff, D. D., Bykov, A. A., Shukurov, A., et al. 1998, MNRAS, 299, 189
Sotomayor-Beltran, C., Sobey, C., Hessels, J. W. T., et al. 2013, A&A, 552, A58
Stovall, K., Ray, P. S., Blythe, J., et al. 2015, ApJ, 808, 156
Sun, X. H., Gaensler, B. M., Carretti, E., et al. 2014, MNRAS, 437, 2936
Sun, X. H., Reich, W., Han, J. L., et al. 2011, A&A, 527, A74
Sun, X. H., Reich, W., Waelkens, A., & Enßlin, T. A. 2008, A&A, 477, 573
Sutinjo, A., O'Sullivan, J., Lenc, E., et al. 2015, RaSc, 50, 52
Taylor, A. R., Gibson, S. J., Peracaula, M., et al. 2003, AJ, 125, 3145
Taylor, A. R., Stil, J. M., & Sunstrum, C. 2009, ApJ, 702, 1230
Taylor, J. H., & Cordes, J. M. 1993, ApJ, 411, 674
Thyagarajan, N., Jacobs, D. C., Bowman, J. D., et al. 2015, ApJ, 804, 14
Tingay, S. J., Goeke, R., Bowman, J. D., et al. 2013, PASA, 30, 7
Trott, C. M. 2014, PASA, 31, e026
Uyanıker, B., Landecker, T. L., Gray, A. D., & Kothes, R. 2003, ApJ, 585, 785
van Haarlem, M. P., Wise, M. W., Gunst, A. W., et al. 2013, A&A, 556, A2
Vinyaikin, E. N., & Paseka, A. M. 2015, ARep, 59, 672
Wayth, R. B., Lenc, E., Bell, M. E., et al. 2015, PASA, 32, e025
Wieringa, M. H., de Bruyn, A. G., Jansen, D., et al. 1993, A&A, 268, 215
Willis, A. G., Mevius, M., Anderson, J. M., et al. 2016, A&C, submitted
Wolleben, M. 2007, ApJ, 664, 349
Wolleben, M., Landecker, T. L., Reich, W., & Wielebinski, R. 2006, A&A, 448, 411
Wright, E. L. 2006, PASP, 118, 1711
Wrobel, J. M., & Walker, R. C. 1999, in ASP Conf. Ser. 180 Synthesis Imaging in Radio Astronomy II, ed. G. B. Taylor, C. L. Carilli, & R. A. Perley (San Francisco, CA: ASP), 171